Surface & Coatings Technology 510 (2025) 132250

Contents lists available at ScienceDirect

Surface & Coatings Technology

journal homepage: www.elsevier.com/locate/surfcoat

Deposition of high-velocity oxygen-fuel (HVOF) coatings on laser-powder bed fused (L-PBF) parts subjected to in-situ laser remelting treatments

Maria Francesca Bonilauri [a,*], Matteo Perini [d], Sasan Amirabdollahian [d], Laura Paglia [e], Giovanni Pulci [e], Francesco Marra [e], Edoardo M. Rossi [f], Luca Lusvarghi [a,b,c], Giovanni Bolelli [a,b,c]

[a] Department of Engineering "Enzo Ferrari", Università di Modena e Reggio Emilia, Via Pietro Vivarelli 10/1, 41125 Modena, MO, Italy
[b] InterMech – MO.RE. Centro Interdipartimentale per la Ricerca Applicata e i Servizi nel Settore della Meccanica Avanzata e della Motoristica, Università di Modena e Reggio Emilia, Via Pietro Vivarelli 2, 41125 Modena, MO, Italy
[c] Consorzio Interuniversitario Nazionale per la Scienza e Tecnologia dei Materiali (INSTM), Local Unit: Università di Modena e Reggio Emilia, Via Pietro Vivarelli 10/1, 41125 Modena, MO, Italy
[d] ProM Facility - Trentino Sviluppo, Via Fortunato Zeni 8, 38068, TN, Italy
[e] Dipartimento di Ingegneria Chimica Materiali Ambiente, Università di Roma - 1 "La Sapienza", Via Eudossiana 18, 00184 Roma, Italy
[f] Università degli studi Roma Tre, Department of Civil, Computer and Aeronautical Engineering, Via Vito Volterra 62, Rome 00146, Italy

ARTICLE INFO

Keywords:
Selective laser melting (SLM)
Thermal spray
Surface treatments
Tensile adhesion
Corrosion resistance

ABSTRACT

In this work, we focused on enhancing the adhesion between High Velocity Oxygen-Fuel (HVOF) sprayed coatings and Laser-Powder Bed Fused (L-PBF) substrates by modifying the substrate surface through in-situ laser remelting treatments. Additionally, we investigated whether deposition on laser-treated substrates affected the coating microstructure and performance. Therefore, WC-10%Co-4%Cr coatings were deposited on AISI 316 L stainless steel substrates in as-built conditions and after two different in-situ laser remelting treatments. All substrates were coated both before and after a pickling treatment. Grit-blasted bulk stainless steel samples served as references.

Laser remelting changed the morphology of the L-PBF surfaces depending on the laser parameters used. The most energetic treatment resulted in more widely spaced grooves and melted the unmelted spherical particles attached to the as-built surface, leading to a more uniform material distribution. These changes influenced the adhesion-cohesion of the coatings. Although all tensile test failures were primarily cohesive, the coatings deposited on the substrates subjected to the most energetic treatment exhibited an increased adhesion-cohesion strength, exceeding 80 MPa, while all other samples showed values around 70 MPa.

When the substrate was subjected to remelting treatments, however, the corrosion resistance of the coated systems decreased due to faster substrate corrosion in areas exposed to corrosive agents penetrating through coating defects.

1. Introduction

Although Additive Manufacturing (AM) technologies are now widely used across various industrial applications, providing a valid alternative to traditional methods in the production of prototypes and components from polymeric, metallic, ceramic, and composite materials, they still present some fundamental challenges that ongoing research attempts to overcome. Poor surface quality is one of the most critical aspects of additively manufactured components. Regardless of the material or technique employed, additively-made components are generally characterized by high surface roughness and poor finish [1–5]. Among the available technologies for metallic materials, powder bed-based techniques allow to reach superior dimensional accuracy and better surface finish [6,7]. Laser-Powder Bed Fusion (L-PBF), also known as Selective Laser Melting (SLM), Laser Beam Melting (LBM), or Direct Metal Laser Sintering (DMLS), is the most advanced and widespread metal-AM technology in the current industrial scenery [8,9]. In terms of surface finish, L-PBF parts typically exhibit rough surfaces, characterized by

* Corresponding author.
E-mail address: mariafrancesca.bonilauri@unimore.it (M.F. Bonilauri).

https://doi.org/10.1016/j.surfcoat.2025.132250
Received 19 March 2025; Received in revised form 5 May 2025; Accepted 6 May 2025
Available online 7 May 2025

Table 1
Nominal chemical composition of the AM 316 L stainless steel powder by F3nice, in wt%.

Cr	Ni	Mo	Mn	Si	C	P	S	Fe
16–18	10–14	2–3	<2	<0.75	<0.03	<0.045	<0.03	Bal.

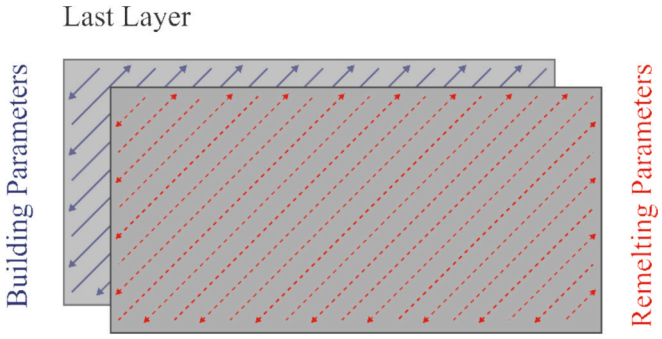

Fig. 1. Scheme of the laser remelting strategy.

Table 2
Sample codes and surface conditions (*AISI 304 wrought samples).

Code	Surface Treatment	Laser Remelting Parameters		
		Power (W)	Scan Speed (mm/s)	Scan Pattern
AB	None	–	–	–
P	Pickling	–	–	–
LRM1	Laser Remelting	90	1500	//
LRM1_P	LRM1 + Pickling	90	1500	//
LRM2	Laser Remelting	95	500	//
LRM2_P	LRM2 + Pickling	95	500	//
W*	Grit-blasted	–	–	–

Table 3
HVOF process parameters. SLPM = Standard Litres Per Minute.

Parameter	Value
Number of torch cycles	3 (pre-heating) + 24 (deposition)
Stand-off distance	240 mm
Pitch distance	6 mm
Gun/substrate relative linear velocity	750 mm/s
H_2 flow rate / pressure	666 SLPM / 965 kPa (110 psi)
O_2 flow rate / pressure	234 SLPM / 1172 kPa (170 psi)
Compressed air flow rate / pressure	235 SLPM / 689 kPa (100 psi)
Equivalence ratio (λ)	0.85
Powder feed rate	60 g/min

average roughness values (Ra) of the order of 10 μm. The main causes behind this poor surface quality are the characteristic layer-by-layer building process, which introduces the so-called staircase or stair-step effect, and the presence of adhered, partially melted powder particles [10,11]. The adhesion of these particles results from the contact of extremely hot surfaces with the powder bed. The presence of an inert gas flow in the building chamber further contributes by moving some particles, which deposit on these hot surfaces [12]. In addition, laser parameters, in association with the response of the material to the energy input, strongly affect the quality of the part, including that of the surfaces. Excessive energy input and too high scanning speeds can develop instability in the melt pool, causing a phenomenon known as balling. It manifests as the breakup of the molten material into droplets, forming spherical or semi-spherical protrusions on the surfaces [11,13,14]. At the same time, at low energy inputs high roughness levels have been reported in the literature, due to the insufficient melting of the powder [15]. An incorrect selection of laser parameters results in a pronounced alternation of peaks and valleys, leading to an uneven surface finish

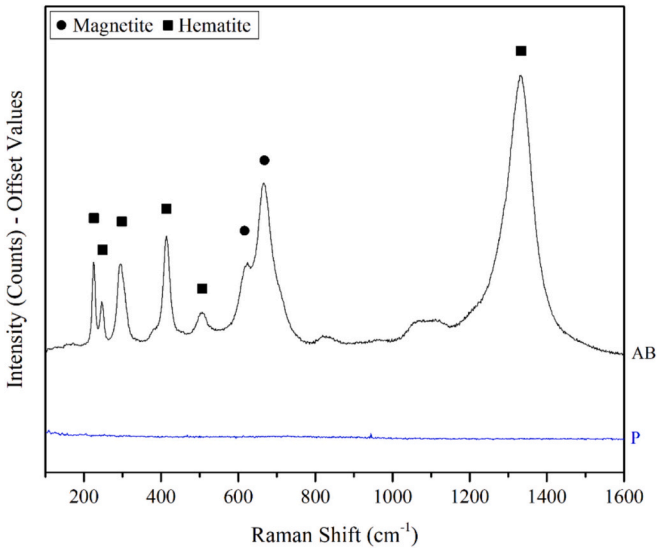

Fig. 2. Comparison between the Raman spectra acquired on the surface of as-built (AB) and pickled (P) samples.

[13,16,17]. However, choosing the optimal set of laser parameters is not sufficient to control surface roughness, as even with consistent laser parameters, changing the scanning strategy can significantly affect the surface appearance [18]. Thus, a proper combination of correct laser parameters and optimized scan strategy is necessary.

Several studies in the literature have shown that remelting the material by the so-called contour strategy can have beneficial effects in terms of roughness, if conducted with the appropriate parameters [13,15,17].

The technique of material remelting is not limited to the contour strategy. Indeed, laser remelting is also used in L-PBF processes to remelt newly consolidated material layers during construction. This technique ensures complete fusion of partially consolidated regions, reducing porosity and modifying the material's microstructure, impacting its micro-mechanical and mechanical properties [19–23]. In addition, remelting has been shown to reduce the balling effect, resulting in smoother surfaces [14]. Laser remelting can also be performed at the end of the construction, targeting the top layer, to influence the surface morphology of the components [19,24]. With this technique, also referred to in the literature as surface laser remelting and, less commonly, as skin scanning, several recent studies reported a variation in the surface morphology of L-PBF parts made of different materials, such as Ti-alloy [19], Al-alloy [25], and steels [18,19].

Scientific research in the field of L-PBF extensively focuses on improving the surface morphology of products because the poor surface finish of these parts negatively affects their performance and durability, impacting their mechanical properties, as well as their tribological and functional characteristics. However, while surface treatments can effectively enhance surface morphology, density, and micro-mechanical properties, their impact on the functional properties of surfaces, such as corrosion and wear resistance, is limited. Consequently, achieving the desired surface characteristics often requires the application of coatings. Particularly relevant to this work are the attempts made over the years regarding the deposition of thermally sprayed coatings on parts produced through powder bed fusion (PBF).

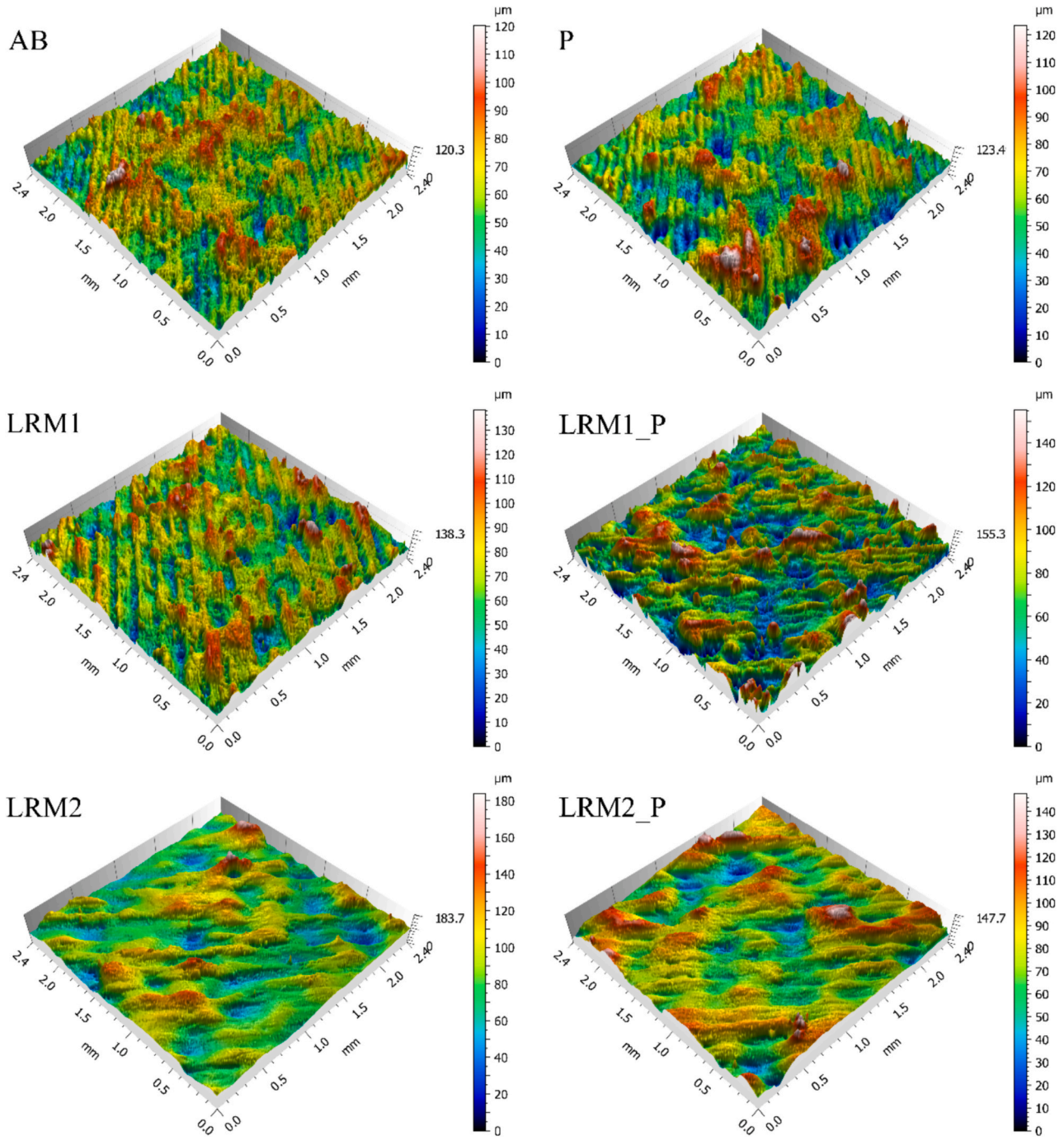

Fig. 3. Comparison of the 3D reconstructions showing the morphology of the L-PBF surfaces in all conditions. The label in each panel refers to the surface condition, following the designation in Table 2.

Starting from the 2010s, these coatings have been successfully applied on PBF parts to reach different objectives, demonstrating their effectiveness in improving the surface characteristics of additively manufactured components. For example, Zafer et al. [26] employed the deposition of thermally sprayed coatings in association with a Hot Isostatic Pressing (HIP) treatment to reduce the surface pores in Ni-superalloy parts made by electron beam-powder bed fusion (EB-PBF). Similarly, Tillmann et al. [27] used High Velocity Oxygen Fuel (HVOF) and HIP to close the surface pores of L-PBF parts. Other authors, however, have also employed the deposition of thermally sprayed coatings to functionalize the surfaces of PBF parts. Recently, Li et al. [28] deposited plasma-sprayed ceramic coatings on L-PBF CoCrMo alloys to increase their wear and corrosion resistance. Jafarlou et al. [29] deposited powder blends of Ni and chromium carbide onto 15-5PH stainless-steel L-PBF parts by cold spraying in order to reduce the surface roughness of the parts and increase their fatigue life. Bellippady et al. [30] deposited thermal barrier coatings (TBCs) on EB-PBF parts, demonstrating that despite the poor surface finish of additively manufactured components, TBCs can be successfully applied on them, without significantly compromising their properties.

One of the reasons thermal spray coatings have gained popularity in recent years for improving the surface properties of PBF components is the possibility to effectively deposit these coatings onto rough surfaces, such as those produced by PBF, achieving good adhesion. Interestingly,

Table 4
Roughness values of all substrates, calculated on the primary surfaces, with no waviness filtering.

		AB	LRM1	LRM2
Sa [μm]	*As-is*	11 ± 1	17 ± 3	14 ± 2
	Pickled	16 ± 2	21 ± 3	18 ± 2
Sq [μm]	*As-is*	14 ± 2	22 ± 3	17 ± 3
	Pickled	21 ± 3	27 ± 4	23 ± 3
Sz [μm]	*As-is*	116 ± 11	146 ± 14	185 ± 33
	Pickled	136 ± 18	167 ± 19	168 ± 25
Ssk	*As-is*	−0.1 ± 0.1	0.1 ± 0.3	−0.1 ± 0.4
	Pickled	0.3 ± 0.1	0.1 ± 0.1	0.3 ± 0.1
Sku	*As-is*	3.3 ± 0.4	3.1 ± 0.3	3.2 ± 0.6
	Pickled	3.3 ± 0.1	3.1 ± 0.2	3.5 ± 0.5
Sp [μm]	*As-is*	59 ± 2	71 ± 8	84 ± 21
	Pickled	73 ± 11	86 ± 17	87 ± 15
Sv [μm]	*As-is*	57 ± 13	74 ± 7	101 ± 12
	Pickled	63 ± 7	81 ± 12	81 ± 12
Sk [μm]	*As-is*	27 ± 1	47 ± 9	28 ± 8
	Pickled	36 ± 5	60 ± 9	39 ± 6
Spk [μm]	*As-is*	11 ± 2	19 ± 5	13 ± 4
	Pickled	19 ± 3	24 ± 9	21 ± 6
Svk [μm]	*As-is*	11 ± 1	21 ± 4	13 ± 4
	Pickled	15 ± 2	23 ± 5	18 ± 4
Sal [μm]	*As-is*	149 ± 37	93 ± 5	200 ± 7
	Pickled	188 ± 8	96 ± 11	200 ± 11
Str	*As-is*	0.7 ± 0.1	0.6 ± 0.1	0.7 ± 0.1
	Pickled	0.7 ± 0.1	0.7 ± 0.1	0.7 ± 0.2
Sdq [°]	*As-is*	52 ± 2	67 ± 5	35 ± 6
	Pickled	44 ± 3	66 ± 2	42 ± 5
Sds [1/μm^2]	*As-is*	0.014 ± 0.001	0.012 ± 0.001	0.013 ± 0.001
	Pickled	0.011 ± 0.001	0.012 ± 0.001	0.012 ± 0.001
Ssc [1/μm]	*As-is*	1.0 ± 0.1	1.7 ± 0.3	0.5 ± 0.1
	Pickled	0.7 ± 0.1	1.8 ± 0.2	0.6 ± 0.1

the rough surfaces typical of PBF parts, often regarded as a defect, can be useful for the adhesion of thermally sprayed coatings, which typically require quite rough surfaces to adhere properly [31].

Zhang et al. [32] were among the first to highlight the critical influence of the surface morphology and roughness on the adhesion of thermally sprayed coatings on additively manufactured parts, studying the adhesion of suspension plasma sprayed (SPS) coatings deposited onto vertically and horizontally built L-PBF surfaces.

Recently, Dlouhá et al. [33] demonstrated that thermal spraying can be performed on L-PBF samples without the need for intermediate surface treatment, obtaining well-adhered coatings.

We also obtained similar conclusions in a previous study [34], in which well-adhered HVOF coatings were deposited on L-PBF substrates both in as-built conditions and subjected to different surface treatments.

Interestingly in [34] we found that while good adhesion could be achieved also on as-built surfaces, the presence of semi-molten particles on L-PBF substrates has an impact on the quality of the coatings. These particles inhibited the proper deposition of some coating splats, leading to the so-called shadow effects, which resulted in localized micro-defects and porosity in the first coating layers. Although these defects did not significantly impact the overall results of the study, their removal could improve the final properties of the substrate-coating system, leading to the reduction or, ideally, the elimination of internal defects near the interface with the substrate. Moreover, the presence of these particles at the interface may impact the stress gradient at the interface between the coating and the substrate, which was found to potentially influence the adhesion of the coating [35].

To remove the semi-molten particles adhered on the surface of L-PBF parts and investigate how the modified surface morphology affects the adhesion of thermally sprayed coatings, in this work, AISI 316 L L-PBF substrates were subjected to two different in-situ surface laser remelting treatments before the deposition of WC-CoCr-based HVOF coatings.

To the authors' knowledge, no studies in the literature have investigated the possibility of laser remelting L-PBF substrates prior to the deposition of such coatings. However, the effectiveness of laser treatments as surface preparation techniques before the deposition of thermally sprayed coatings has been widely demonstrated [36]. In particular, laser texturing has been employed in several studies as an alternative to grit-blasting to enhance the adhesion and properties of plasma sprayed [37], cold sprayed [38], and HVOF [39–41] coatings. Although this technique affects the substrate surface differently from laser remelting, creating patterns of holes rather than redistributing the material, both these laser treatments alter the surface morphology and roughness. Therefore, it is possible that laser remelting could also serve as a surface preparation technique before the deposition of thermally sprayed coatings.

The aim of this work was therefore to assess whether the morphological changes induced by laser remelting on the surface of L-PBF samples influenced the adhesion/cohesion, the microstructure, and the performance of HVOF deposited coatings. For this purpose, the tensile adhesion (ASTM C633) strength, the cyclic impact response, and the corrosion resistance of HVOF coatings deposited onto L-PBF samples subjected to two different in-situ laser remelting treatments were

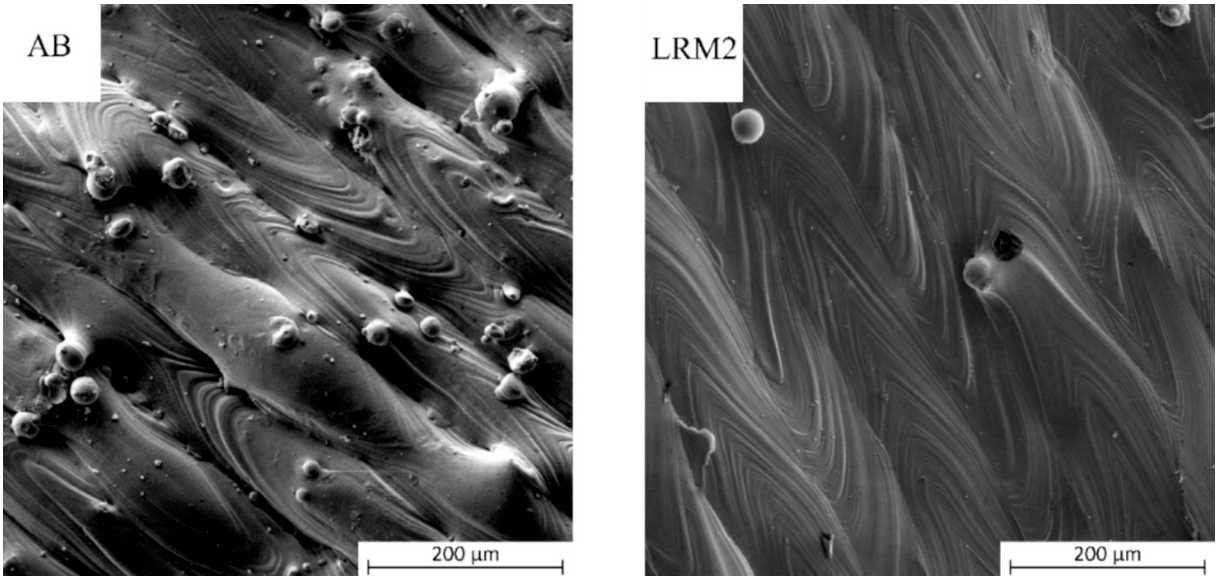

Fig. 4. SEM micrographs acquired in secondary electrons mode on the surfaces of an AB and an LRM2 sample.

Table 5
Waviness and roughness values of substrates with different surface treatment conditions, not subjected to pickling. All values were calculated after the application of a Gaussian filter (cut-off value = 80 μm).

		AB	LRM1	LRM2
Sa [μm]	*Wav.*	9.6 ± 1.2	15.2 ± 2.1	13.1 ± 1.9
	Rough.	2.5 ± 0.1	3.9 ± 0.6	1.3 ± 0.2
Sq [μm]	*Wav.*	12.2 ± 1.6	19.3 ± 2.7	16.5 ± 2.6
	Rough.	3.7 ± 0.2	5.8 ± 0.9	2.2 ± 0.5
Sz [μm]	*Wav.*	91.5 ± 18.8	125.8 ± 17.8	152.0 ± 4.4
	Rough.	93.5 ± 3.5	121.5 ± 13.0	124.8 ± 47.5
Ssk	*Wav.*	−0.1 ± 0.2	0.1 ± 0.1	−0.1 ± 0.5
	Rough.	0.2 ± 0.2	−0.3 ± 0.2	−0.5 ± 0.5
Sku	*Wav.*	3.3 ± 0.6	3.0 ± 0.3	3.0 ± 0.6
	Rough.	10.6 ± 1.1	9.8 ± 1.0	38.4 ± 27.2
Sp [μm]	*Wav.*	47.0 ± 7.9	63.1 ± 10.5	75.8 ± 19.6
	Rough.	47.5 ± 2.0	57.0 ± 5.5	47.9 ± 16.9
Sv [μm]	*Wav.*	44.5 ± 14.8	62.8 ± 7.4	75.2 ± 15.1
	Rough.	46.0 ± 5.5	64.5 ± 8.5	76.9 ± 30.7
Sk [μm]	*Wav.*	23.0 ± 0.7	41.1 ± 7.8	26.1 ± 6.8
	Rough.	5.8 ± 0.5	9.2 ± 1.8	3.0 ± 0.6
Spk [μm]	*Wav.*	9.4 ± 1.6	16.1 ± 4.2	11.8 ± 3.9
	Rough.	4.9 ± 0.1	8.1 ± 1.5	3.1 ± 1.2
Svk [μm]	*Wav.*	8.5 ± 1.4	16.5 ± 2.8	11.1 ± 3.8
	Rough.	5.9 ± 0.2	9.8 ± 2.0	3.9 ± 0.9
Sal [μm]	*Wav.*	167.1 ± 34.2	108.2 ± 7.4	207.1 ± 2.5
	Rough.	11.6 ± 0.2	12.4 ± 0.2	12.5 ± 0.6
Str	*Wav.*	0.8 ± 0.1	0.6 ± 0.1	0.7 ± 0.1
	Rough.	0.4 ± 0.1	0.5 ± 0.1	0.2 ± 0.1
Sdq [°]	*Wav.*	14.9 ± 0.6	26.0 ± 3.5	14.1 ± 3.2
	Rough.	50.1 ± 2.2	66.1 ± 5.2	32.5 ± 5.9
Sds [1/μm^2]	*Wav.*	$4.0 \times 10^{-5} \pm 0.1 \times 10^{-6}$	$4.0 \times 10^{-5} \pm 0.1 \times 10^{-6}$	$1.0 \times 10^{-5} \pm 0.1 \times 10^{-6}$
	Rough.	0.017 ± 0.001	0.016 ± 0.001	0.018 ± 0.001
Ssc [1/μm]	*Wav.*	$1.2 \times 10^{-2} \pm 0.1 \times 10^{-3}$	$2.0 \times 10^{-2} \pm 0.1 \times 10^{-3}$	$0.7 \times 10^{-2} \pm 0.1 \times 10^{-3}$
	Rough.	0.9 ± 0.1	1.7 ± 0.3	0.4 ± 0.1

compared with those of the same coatings deposited on as-built substrates, as well as with coatings sprayed on conventionally machined and grit-blasted substrates. Regardless of the surface finishing (as-built or laser remelted), the L-PBF samples were coated both before and after undergoing a pickling treatment, to remove surface oxides, which were found to influence the adhesion of similar coatings in [34].

To understand the causes behind potential variations in the behaviour of different samples, the results of the various tests were accompanied by SEM-EDX investigations, optical profilometry analyses, Raman spectroscopy analyses, X-Ray Diffraction (XRD) measurements, instrumented microhardness testing, and TEM analyses.

2. Experimental

2.1. Manufacturing of L-PBF samples

L-PBF samples were built using the AM 316 L powder by F3nice (F3nice Srl, Oslo; NO) with the nominal chemical composition (in wt%) shown in Table 1.

The particle size distribution of the powder, experimentally determined by laser diffraction (Malvern Mastersizer 2000 with Hydro-2000S wet dispersion unit, Malvern Instruments, Malvern, UK), was characterized by d_{10} = 22.2 μm, d_{50} = 32.0 μm, and d_{90} = 46.0 μm.

L-PBF samples were produced using a Concept Laser Mlab Cusing (General Electric, Boston, Massachusetts, USA) equipped with a 100 W fibre laser, operating under an inert (Ar) atmosphere with an O_2 content below 0.3 %.

A layer thickness of 25 μm was employed.

The samples comprised plates measuring 60 × 25 × 3 mm^3, employed for every characterization test except for tensile adhesion testing, for which Ø 26.5 mm × 38.3 mm height cylinders were built. All the surfaces to be coated were grown horizontally, meaning parallel to the building platform. Our previous research [34] indeed showed that there was no significant difference between the adhesion and properties of HVOF-sprayed WC-CoCr coatings deposited onto surfaces grown parallel or perpendicular to the building platform.

Once detached from the building platform, the cylinders underwent turning along the cylindrical surface and grinding on the bottom face to obtain final external dimensions of Ø 25.4 ± 0.1 mm × 38.1 ± 0.1 mm height, in compliance with the specifications and tolerances required by the ASTM C633–13 standard. In addition, an M16 × 1.5 threaded blind hole with a depth of 20 ± 1 mm was drilled on the bottom face to accommodate a threaded bar within the cylinder. This bar is necessary for fixing the samples in the tensile testing machine.

2.2. Surface treatments

Samples were tested under six distinct surface conditions:

- As-built (AB), meaning without any additional surface treatments.
- Pickled (P) to remove any surface oxide layer. Pickling was conducted in a commercial solution (Ricerca Chimica S.r.l., Vighizzolo d'Este, Italy) typically used in the industrial pickling of welded AISI 316 L stainless steel.
- Laser Remelted with a laser power of 90 W and a scanning speed of 1500 mm/s (LRM1). This treatment was performed within the L-PBF building chamber immediately after the sample building. Following the consolidation of the last layer, an additional laser scan over the surface induced material remelting. The scan strategy was parallel to that of the newly consolidated layer (Fig. 1).
- Subjected to LRM1, as described above, and pickled (LRM1_P).
- Laser Remelted with a different set of laser parameters (LRM2). This treatment was performed as for the LRM1 treatment (Fig. 1), employing higher laser power (95 W) and lower scanning speed (500 mm/s) to achieve higher energy input than the LRM1 treatment.
- Subjected to LRM2, as described above, and pickled (LRM2_P).

The laser parameters for the remelting treatments were selected based on preliminary, simplified experiments, in which the surfaces of samples similar to those used in this study were subjected to in-situ laser remelting with variations in laser power, speed, and hatch distance. The surface modifications induced by these treatments were evaluated through SEM observations. Based on these observations, parameter sets employing the same hatch distance as the consolidation parameters were chosen to minimize the number of additional variables. Subsequently, power-speed combinations were selected to achieve, in one case, a significant alteration in the morphology and appearance of the L-PBF surfaces (LRM2), and, in the other, only slight changes in the surface appearance (LRM1).

For comparison purposes, wrought (W) AISI 304 stainless steel plates and cylinders (obtained by cutting and machining extruded commercial products) were used. These were grit-blasted with a manual blasting machine operated using 36 mesh corundum at 5 bar pressure. Due to the similarity in mechanical properties, it is believed that the use of AISI 304 wrought references instead of AISI 316 L ones would not significantly alter the results of the adhesion tests (see Section 2.4).

The conditions of the samples are summarized in Table 2.

2.3. Deposition of the HVOF coatings

The deposition of the HVOF coatings followed the same procedure described in [34].

The feedstock material for the coatings was a WC-10%Co-4%Cr (in wt%) powder (Woka 3652, Oerlikon Metco, Immelborn, Germany). Its particle size distribution, previously determined via laser diffraction in [34], was characterized by d_{10} = 25.5 μm, d_{50} = 40.7 μm, and d_{90} = 64.6 μm.

WC-10%Co-4%Cr coatings were deposited using a Diamond Jet 2600

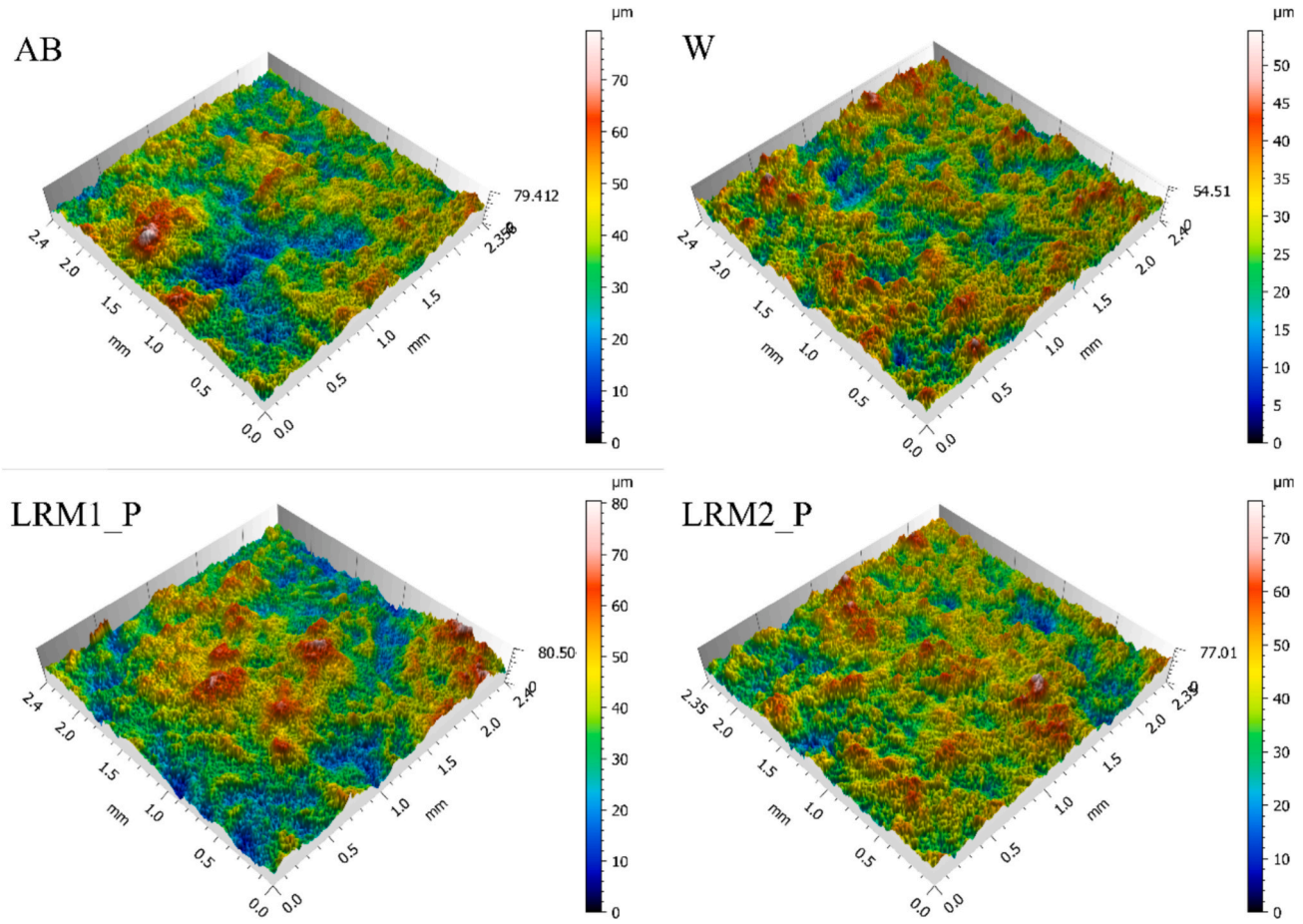

Fig. 5. 3D reconstructions showing the surface morphology of coated samples. The label in each panel refers to the substrate surface condition, following the designation in Table 2. W: wrought and grit-blasted reference sample.

(Oerlikon Metco, Wohlen, CH) High Velocity Oxygen-Fuel (HVOF) spraying system equipped with a H_2-fuelled DJ8H gun (hybrid air-water cooling).

Before the coating deposition, all samples, regardless of the surface condition, were ultrasonically cleaned in acetone and dried with compressed air. Samples were mounted on a turntable with a horizontal axis using suitable fixtures and rotated in front of a horizontally traversing gun to achieve the desired values of gun-substrate linear speed and pitch distance. Complete process parameters are listed in Table 3, and were the same as in [34].

To cool the samples and remove any overspray between successive gun passes, fixed air jets were employed.

The deposition process involved three pre-heating cycles with identical kinematics and gas flow rates but without powder feed, followed by 24 deposition cycles with powder feed. Every three deposition cycles, the process was interrupted for a 20 s-period while the turntable kept rotating in front of the fixed air jets, to cool down the samples.

The deposition efficiency, expressed as the ratio of the experimental mass gain of the plates after spraying (measured by weighing two plates before and after deposition for every run, using an analytical scale with a $\pm$ 0.01 g accuracy) over the computed mass of powder sprayed toward a plate during the coating process, was in the range of 60–69 % during all runs.

2.4. Characterizations and testing

The surface profile of the substrates under all pre-treatment conditions, as well as that of the coated samples, was characterized using a non-contact profilometer operating in structured illumination mode (ConfoSurf, ConfoVis GmbH, Jena, Germany) coupled with an optical microscope (Nikon Eclipse LV150N). The microscope was set with a 10× objective and acquisitions were performed over 2.4 × 2.4 mm^2 areas. At least three areas were acquired at random locations on the samples and the results were averaged.

Relevant roughness parameters that were measured were Sa (arithmetic mean height), Sq (root mean square height), Sz (maximum profile height), Sp and Sv (maximum peak height and maximum valley depth), Ssk (skewness of the profile heights distribution), Sku (kurtosis of the profile heights distribution), Sk, Spk, and Svk (core height, reduced peak height, and reduced valley depth obtained by processing the Abbot curve), Sal (auto-correlation length, which provides an approximate estimate of the average wavelength of the profile), and Str (texture aspect ratio, which is a measure of the spatial isotropy or orientation of the surface texture, with Str = 1 indicating a fully isotropic texture and Str → 0 when the surface features are fully oriented along a single direction). All these parameters were measured according to ISO 25178.

In addition, Sds (summit density) and Ssc (mean summit curvature) were also measured according to the EUR 15178 N standard.

All the mentioned parameters were extracted starting both from the primary surfaces (with planarity correction) and after the application of a waviness filter. Specifically, a Gaussian filter compliant with the ISO 16610-61 standard, with a cut-off value of 80 µm, was applied to discern the individual contributions of roughness and waviness.

The surfaces' quality and conditions were examined considering both morphology and surface roughness, and the presence of surface oxides. Therefore, to characterize any oxide layer that might exist on the L-PBF surfaces, micro-Raman spectroscopy (LabRam spectrometer, Horiba Jobin-Yvon, Longjumeau, France) was conducted, using a 532 nm-

Table 6
Roughness values of all coated samples (W = grit-blasted stainless steel plate). All values were calculated on the primary surfaces, with no waviness filtering.

		AB	LRM1	LRM2	W
Sa [μm]	*As-is*	8.7 ± 0.9	9.2 ± 0.5	7.4 ± 0.7	5.3 ± 0.3
	Pickled	7.7 ± 1.5	9.8 ± 0.5	7.7 ± 0.8	
Sq [μm]	*As-is*	11.0 ± 1.1	11.7 ± 0.7	9.3 ± 0.8	6.6 ± 0.3
	Pickled	9.6 ± 2	12.4 ± 1.0	9.7 ± 1.0	
Sz [μm]	*As-is*	82.6 ± 7.8	93.0 ± 10.7	73.3 ± 6.7	56.9 ± 2.7
	Pickled	73.9 ± 8.5	91.4 ± 12.8	79.7 ± 3.8	
Ssk	*As-is*	0.3 ± 0.3	0.3 ± 0.3	0.1 ± 0.1	0.1 ± 0.1
	Pickled	0.1 ± 0.2	0.2 ± 0.1	0.1 ± 0.1	
Sku	*As-is*	3.4 ± 0.6	3.2 ± 0.4	3.0 ± 0.3	3.0 ± 0.1
	Pickled	3.1 ± 0.3	3.3 ± 0.8	3.2 ± 0.2	
Sp [μm]	*As-is*	46.8 ± 7.6	50.9 ± 9.2	38.8 ± 5.0	29.2 ± 2.1
	Pickled	39.7 ± 4.6	50.5 ± 11.6	40.3 ± 3.2	
Sv [μm]	*As-is*	35.9 ± 0.2	42.1 ± 1.6	34.5 ± 1.7	27.7 ± 0.6
	Pickled	34.2 ± 3.9	40.9 ± 3.2	39.4 ± 0.7	
Sk [μm]	*As-is*	16.1 ± 0.5	17.5 ± 1.6	16.5 ± 0.2	13.5 ± 0.5
	Pickled	15.5 ± 0.6	17.0 ± 0.8	16.7 ± 0.4	
Spk [μm]	*As-is*	7.2 ± 2.1	7.2 ± 0.1	6.5 ± 0.7	5.2 ± 1.0
	Pickled	6.1 ± 0.6	6.6 ± 0.5	7.2 ± 0.4	
Svk [μm]	*As-is*	5.1 ± 0.6	5.8 ± 0.4	6.2 ± 0.5	5.2 ± 0.5
	Pickled	5.8 ± 0.7	6.0 ± 0.3	6.2 ± 0.1	
Sal [μm]	*As-is*	287.7 ± 12.1	292.5 ± 41.5	193.6 ± 38.0	129.3 ± 10.1
	Pickled	229.0 ± 48.8	344.9 ± 33.2	215.9 ± 43.0	
Str	*As-is*	0.8 ± 0.1	0.7 ± 0.1	0.8 ± 0.1	0.8 ± 0.1
	Pickled	0.6 ± 0.1	0.6 ± 0.1	0.7 ± 0.1	
Sdq [°]	*As-is*	30.1 ± 0.5	31.8 ± 0.8	32.9 ± 0.2	29.3 ± 0.1
	Pickled	29.9 ± 0.1	30.9 ± 0.4	33.0 ± 0.3	
Sds [1/μm^2]	*As-is*	1.3×10^{-2}	1.2×10^{-2}	1.3×10^{-2}	1.3×10^{-2}
	Pickled	$\pm 0.1 \times 10^{-3}$	$\pm 0.1 \times 10^{-3}$	$\pm 0.1 \times 10^{-3}$	$\pm 0.1 \times 10^{-3}$
Ssc [1/μm]	*As-is*	0.46 ± 0.01	0.47 ± 0.05	0.53 ± 0.01	0.45 ± 0.01
	Pickled	0.46 ± 0.01	0.47 ± 0.01	0.52 ± 0.01	

wavelength laser emitted from a solid-state source and focused on the sample through a 100× objective.

Cross-sections of the coatings were obtained by cutting the plate samples using a semi-automatic metallographic machine (Micromet SA, Remet Sas, Casalecchio di Reno, Italy) with a resin-bound Al_2O_3 abrasive disc. During cutting, the samples were consistently positioned with respect to the wheel to ensure that the stresses on the coating were mainly compressive, thereby preventing detachments and cracks caused by tensile stresses. Subsequently, after hot-mounting in a phenol resin, the cross-sections were ground with SiC papers (from P400 to P4000) or with diamond grinding discs (P600 and P1200) followed by SiC papers (P2500 and P4000). A fair amount of material was removed to eliminate any areas potentially damaged by the cutting operations. Finally, they were polished using a colloidal silica suspension (~60 nm size).

Cross-sectional samples were observed by optical microscopy (Olympus GX51 – Olympus, Tokyo, JP) and scanning electron microscopy (SEM – Nova NanoSEM 450, FEI-Thermo Fisher Scientific, Eindhoven, NL) equipped with an energy-dispersive X-ray (EDX) spectroscopy system (Quantax-200, Bruker Nano GmbH, Berlin, Germany).

Resin-embedded samples for SEM analyses were mounted on Al stubs and sputter-coated with a ~ 10 nm thick Au layer to avoid charge accumulation artefacts.

Using scanning electron microscopy, at least five thickness measurements in various regions along the sections of the coatings were acquired. The results relating to the coatings' thickness were expressed in terms of the average value and standard deviation of these measurements.

The coating-substrate interface was also observed by transmission electron microscopy (TEM: Talos F200S G2, Thermo Fisher Scientific). For this purpose, thin slices were extracted from the interface area of the polished cross-sections of an as-built sample and a pickled one, using focused ion beam (FIB). A Helios Nanolab 600 dual-beam machine (FEI - Thermo Fisher Scientific) was used. The extraction involved depositing a 2 μm-thick protective carbon layer on the area of interest, using a 93 pA ion current. Two regular slices with dimensions of 20 μm × 17 μm were obtained using a 6.2 nA current. The slices were then further processed to achieve a thickness of <100 nm using a 0.46 nA current. Once obtained, the slices were mounted on copper supports. TEM observations were carried out at 200 kV electron beam acceleration voltage, in both TEM and STEM (high-angle annular dark-field – HAADF – detector) modes.

The crystalline phases present in the coatings and any phase changes compared to the feedstock powder were examined using an X-Pert PRO diffractometer (Panalytical, Almelo, NL) equipped with a Cu-Kα radiation source operating at 40 kV and 40 mA. Measurements were conducted in Bragg-Brentano geometry, employing a rapid solid-state detector (X'Celerator). The pattern was acquired for 2θ angles ranging between 30° and 80°, with a scanning step of 0.017° and a counting time of 120 s/step. Results were analysed using High Score Plus software (Panalytical).

The microhardness and elastic modulus of the coatings were measured using depth-sensing Vickers micro-indentation (MCT indenter, Anton Paar – TriTec, Corcelles, CH). Thirty indentations were performed on each sample, using a 3 N load, with 4.5 N/min loading/unloading rate and 15 s holding at maximum load. The data were analysed according to ISO 14577-1, and the results were expressed as indentation hardness (H_{IT}) and indentation modulus (E_{IT}) in terms of average ± standard deviation.

Tensile adhesion tests were performed according to the ASTM C633–13 standard. Coated cylindrical samples were glued to uncoated cylinders using an adhesive and a steel frame to ensure sample-counterpart alignment. The LOCTITE® EA 9658 AERO glue, cured at 177 ± 2 °C for 60 min, was employed. Preliminary tests on uncoated cylinders indicated that the adhesion strength of the glue was approximately 100 MPa. The glued cylinders were mounted with a self-aligning system on an Instron 5584 testing device, equipped with a 150 kN load cell. The system was pre-loaded to 5 MPa at 5 mm/min and subsequently

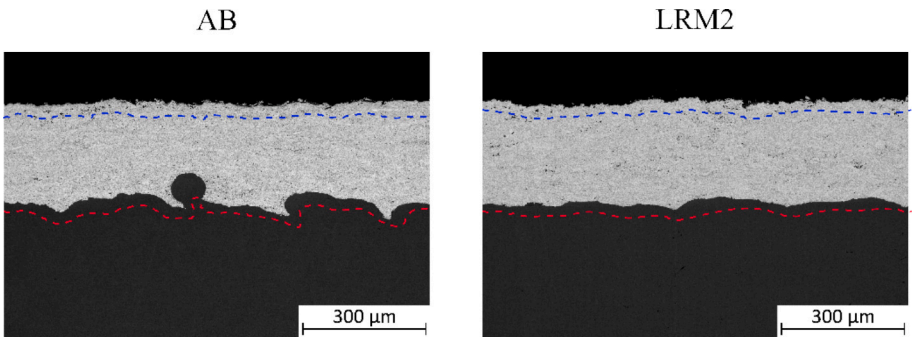

Fig. 6. Cross-sectional micrographs of the coatings deposited onto an AB and an LRM2 sample. The red dashed lines outline the profile of the substrates, while the blue dashed lines follow the profile of the coatings.

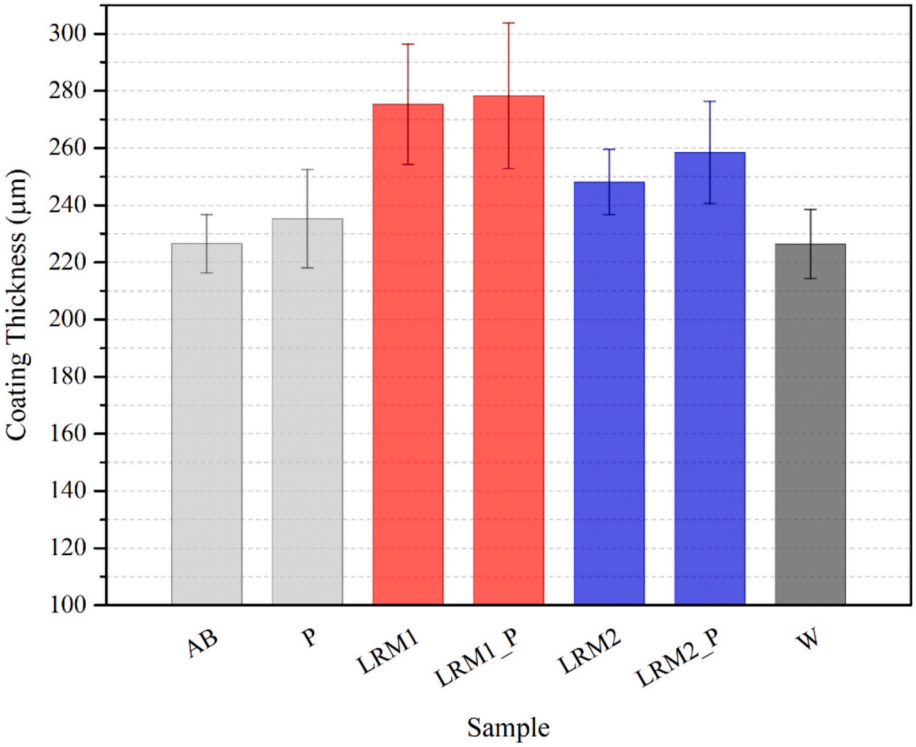

Fig. 7. Coating thickness values. For each sample condition, the histogram shows the average and standard deviation of at least 5 thickness measurements taken in various areas of the cross-sections of the coatings using SEM.

pulled at 10 mm/min until rupture. At least three cylinders per sample type were tested. The fracture location was assessed by optical inspection of broken samples. In addition, cross-sections of selected samples were observed by SEM. For cross-sectional preparation, the samples were cut with a semi-automatic metallographic machine to reduce their dimensions, then the reduced samples were cold-mounted in a transparent epoxy resin and cut along the cross-section with the same semi-automatic metallographic machine. They were ground and polished as described previously.

In addition to tensile adhesion testing, adhesion/cohesion was further characterized using a cyclic impact procedure described in [34]. This test involves repeatedly dropping a 39 mm-diameter X200Cr13 steel ball, fixed to an aluminium crossbar moving vertically along linear roller guides, onto a planar sample. A total of 100 impacts were carried out from an 80 mm drop height, with an overall mass of 1.36 kg (ball + crossbar). For this purpose, samples measuring approximately 25 × 25 mm^2 were cut from the coated plates. Then, they were ground using diamond-based discs (P120 to P1200 abrasive size) and pads with 9 μm and 3 μm polycrystalline diamond suspensions. Finally, they were polished using a cloth with a 3 μm polycrystalline diamond suspension. Three to four tests were performed on each sample. The surfaces were inspected by OM, while the cross-sections of selected samples were observed by SEM. For cross-sectional preparation, the samples were first cold-mounted in a transparent epoxy resin, then cut with a semi-automatic metallographic machine. They were ground and polished as described above.

To test the corrosion resistance of the coatings, electrochemical polarization tests were performed on polished samples measuring approximately 25 × 25 mm^2 (the sample preparation procedure was the same as for the cyclic impact tests). A three-electrode cell with a Pt mesh as counter-electrode and an Ag/AgCl/$KCl_{(sat.)}$ reference electrode was employed. The cell was filled with 300 ml of a 3.5 % (*w/v*) NaCl aqueous solution. The exposed surface area of the working electrode, i.e. the polished specimen, was 1 cm^2. Tests were carried out in aerated conditions at room temperature. Samples were kept in contact with the solution for 1 h in free corrosion conditions, to stabilize the open circuit potential (OCP). Then, an overpotential scan ranging from −0.4 V to +1.6 V vs. OCP at a 0.5 mV/s rate was applied. Two tests were performed on each sample. The corrosion current density and corrosion potential were obtained by linear Tafel fits to the anodic and cathodic curves. Similar analyses were also performed on polished substrates. After the polarization test, the cross-sections of selected coated samples were prepared as described for the previous tests and observed by SEM.

To qualitatively evaluate the corrosion resistance, the coated samples also underwent the corrodkote test following the ASTM B380-97 standard. A corrosive slurry was applied to the surface of the samples, previously polished as described for cyclic impact samples. In addition, a silicone glue was applied around the edges of the coated samples to prevent slurry leakage and to avoid direct contact of the corrosive slurry with the substrates. The slurry consisted of 60 g of ceramic grade kaolin mixed with 100 ml of a corrosive aqueous solution containing NH_4Cl (20 g/l), $FeCl_3{\cdot}6\ H_2O$ (3.3 g/l), and $Cu(NO_3)_2{\cdot}3\ H_2O$ (0.7 g/l). Maintained at a constant temperature (38 ± 2 °C) and humidity (90 % R.H.) in a climatic chamber, the samples were exposed to the slurry for 20 h. At the end of the 20 h-cycle the slurry was removed using water, and the samples were dried with compressed air. A visual inspection was performed to qualitatively assess corrosion. Fresh slurry was then reapplied for a new 20 h-test cycle. The process was repeated for 5 complete cycles, resulting in a total corrosion time of 100 h.

3. Results and discussion

3.1. Surface features of substrates and coatings' surface morphology

The surfaces of the L-PBF samples were analysed by means of Raman spectroscopy, obtaining the spectra in Fig. 2, confirming the presence of a surface oxide scale on the non-pickled samples. The spectrum of this oxide exhibited peaks characteristic of hematite and some peaks of magnetite, which were matched by comparison with reference spectra from the RRUFF database [42]. All pickled samples exhibited almost

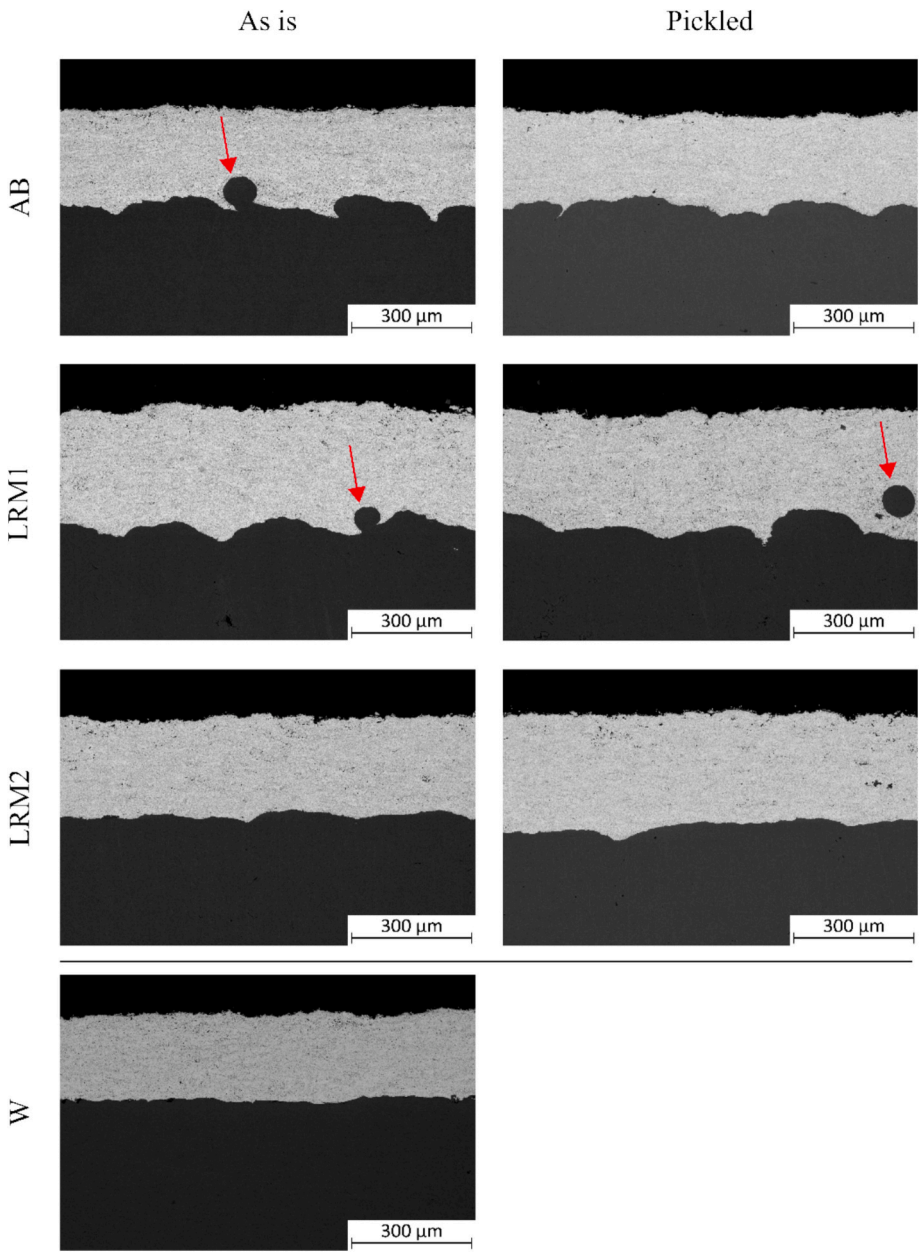

Fig. 8. Low-magnification SEM micrographs (backscattered electrons) of the cross-sections of WC-CoCr coatings onto all substrates.

Table 7
Results of depth-sensing Vickers micro-indentation on the cross-section of HVOF-sprayed WC-CoCr coatings deposited onto the pickled samples: indentation hardness (H_{IT}) and indentation modulus (E_{IT}).

Sample	H_{IT} [GPa]		E_{IT} [GPa]	
	Mean	Std. Dev.	Mean	Std. Dev.
P	14.4	3.1	220	21
LRM1_P	13.8	2.0	250	18
LRM2_P	13.3	2.6	280	19

featureless spectra (as shown in Fig. 2), indicating the absence of an oxide scale on these samples. These results proved that pickling effectively removed the oxide from the surfaces of all L-PBF samples.

The appearance of the L-PBF samples' surfaces is shown in Fig. 3, which compares the 3D reconstructions obtained by the optical profilometry measurements. The left column displays the surfaces not subjected to pickling, while the right column shows the corresponding pickled surfaces. The comparison between the 3D reconstructions in the left column highlights the effects of the two laser remelting treatments performed on the samples.

The surfaces in as-built conditions exhibited strong directionality in the distribution of peaks and valleys, attributed to the scanning direction of the laser. Peaks and valleys appear aligned along parallel lines. Occasionally, 3D reconstructions revealed material accumulations protruding from the surface, most likely derived from unmelted or semi-molten powder particles adhering to the surface [43,44]. These protrusions disrupted the regularity of the pattern formed by the passes of the laser, leading to Str values (Table 4) that deviated from unity probably less than would be expected for highly oriented surface morphologies.

The LRM1 samples exhibited higher average surface roughness values compared to the as-built conditions, while the Sa value of the LRM2 samples, considering the error range associated with the measurements, was similar to that of the AB samples (Table 4).

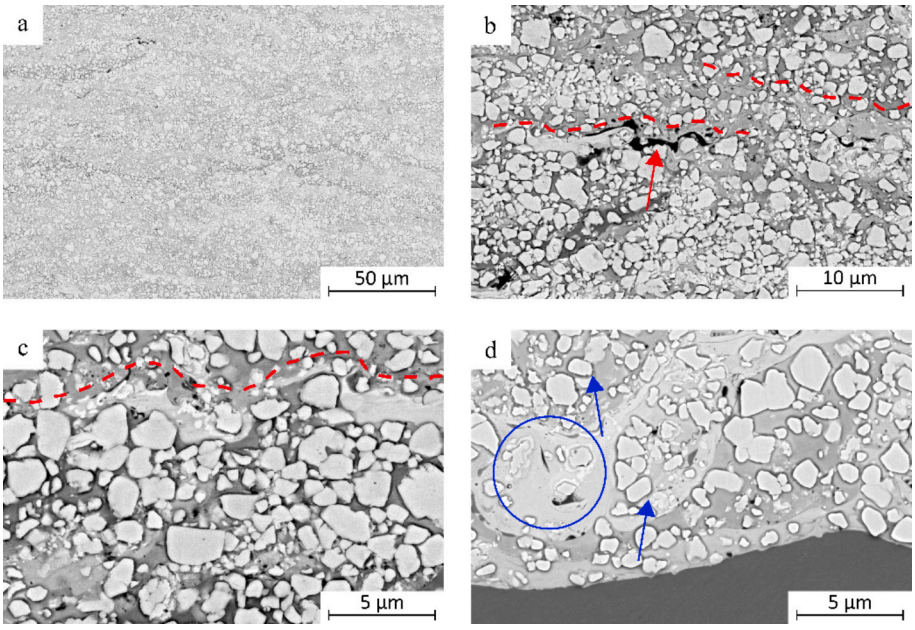

Fig. 9. Higher-magnification SEM micrographs (backscattered electrons) showing the cross-sections of the coating deposited on a P sample (a, b, c) and a W sample (d). The red dashed lines in panels b and c outline splat boundaries. The red arrow in panel b indicates a porosity along a splat boundary. The blue arrows in panel d indicate some visibly rounded carbide particles. The blue circle in panel d highlights some carbide particles surrounded by lighter areas.

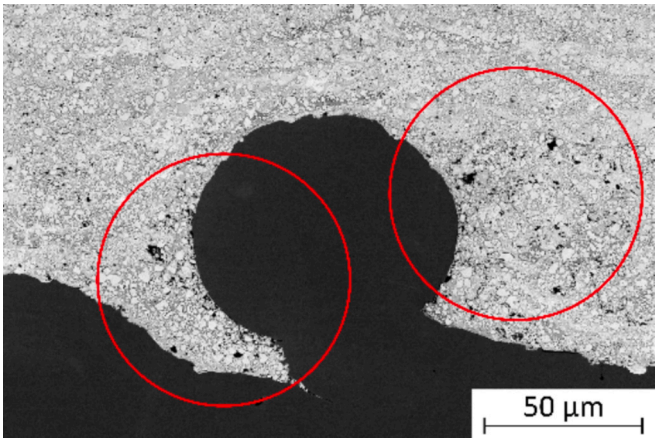

Fig. 10. Detail of the cross-section of the coating on an AB sample. The red circles highlight some defects located near the coating-substrate interface, resulting from "shadow effects" around an unmelted particle protruding from the substrate surface. SEM micrography acquired in backscattered electrons.

After both laser remelting treatments, the pattern of alternating parallel peaks and valleys remained visible on the surface of the samples. However, while the surfaces treated with lower energy density (LRM1) still exhibited protrusions of material interrupting the laser passes' pattern, related to adhered spherical particles, these were less discernible on the LRM2 surfaces (Fig. 3). The higher thermal energy transmitted by the laser to the material, due to the combination of higher laser power and lower scanning speed (see Table 2), likely resulted in the melting of most of the powder particles attached to the surface. This was confirmed by the SEM micrographs acquired on the sample surfaces shown in Fig. 4. Similar results were also reported by Liu et al., who processed AISI 316 L downskin surfaces with a post-building laser polishing treatment [44]. These observations highlight that different laser parameters strongly influence the final surface morphology of laser treated parts. Indeed, several authors in the literature demonstrated that the proper selection of laser parameters is crucial to obtain the desired surface morphology. For instance, in [19], Yasa et al. obtained the lowest roughness values on AISI 316 L samples by employing a laser remelting treatment with low scan speed values and medium laser power values. On the other hand, higher scan speeds or extreme laser power values (either too high or too low) resulted in less effective roughness reduction. Similarly, in a research by Schanz et al. [45] a notable reduction in the surface roughness of AlSi10Mg L-PBF samples was obtained through a post-building laser treatment performed in argon atmosphere. The authors observed that surface roughness was minimized at a certain value of laser intensity (kW/mm^2), while further increases in intensity worsened the result [45].

In general, pickling slightly increased the roughness of the surfaces on which it was applied (Table 4), without significantly altering their morphology, as also observed in [34]. This was confirmed by the fact that the Ssk and Sku parameters, which describe the shape of the height distribution curve, were not modified by pickling, nor were the autocorrelation length Sal, which gives a measure of the shortest "wavelength" of the surface features, and the Str parameter reflecting the degree of orientation of the surface texture.

As mentioned in Section 2.4, to better describe the effects of the remelting treatments, the roughness parameters were also calculated after applying a waviness filter. This procedure allowed to distinguish between the contributions of waviness and roughness. In particular, the laser scanning pattern could be effectively captured by the waviness profile and was decoupled from the finer-scale roughness within each laser track, which was described by the filtered roughness profile. Table 5 presents the values of the parameters divided between waviness and roughness for the non-pickled samples, as it seems that pickling did not significantly change the results.

As suggested by the 3D reconstructions in Fig. 3, the remelting treatment with higher energy input (LRM2) apparently increased the distance within which the pattern of peaks and valleys repeats. This resulted in a surface where material peaks appear more spaced apart, leading to a more uniform distribution of the material across the surface. On the other hand, the treatment with lower energy input seems to have resulted in a surface where the pattern repeated with slightly smaller distances. This was proven by the Sal values associated with surface waviness (Table 5), which were higher for the LRM2 samples and lower

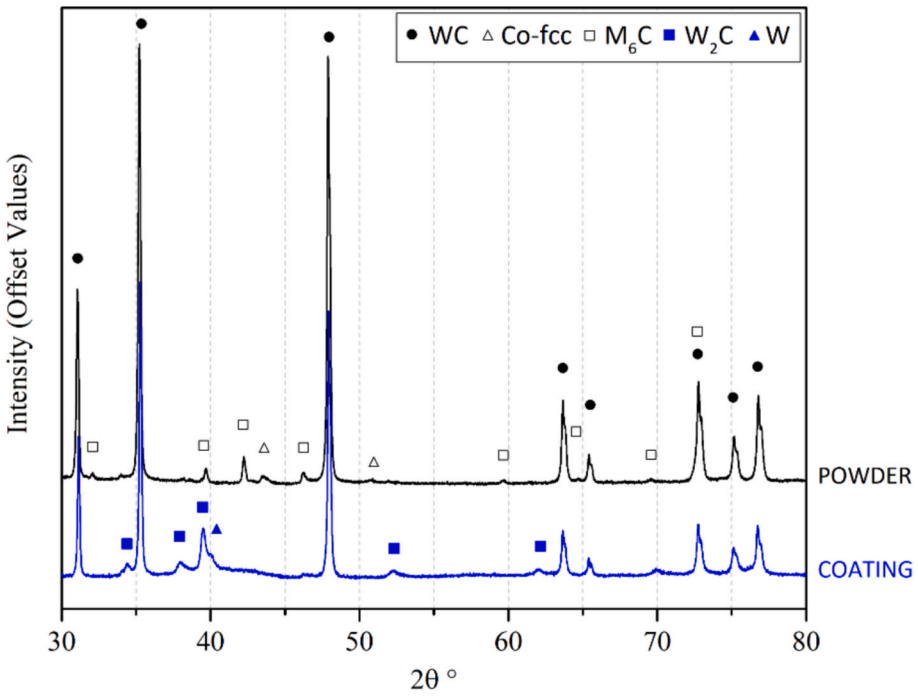

Fig. 11. XRD patterns of the feedstock powder (black line) and the coating (blue line). Reference patterns: WC (JCPDF 51-939), Co-fcc (JCPDF 15-806), M6C (JCPDF 27-1125), W2C (JCPDF 37-776), W (JCPDF 4-806).

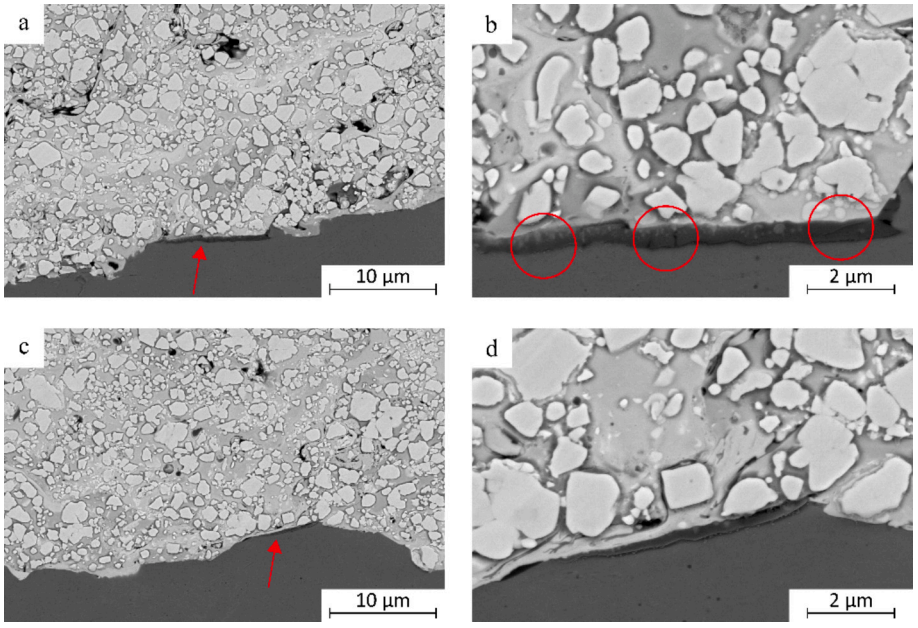

Fig. 12. SEM micrographs (backscattered electrons) showing details of the coating-substrate interface in the AB (a, b) and LRM1 sample (c, d). Red arrows = interface oxide. Red circles = cracks.

for the LRM1 samples compared to the AB samples. Additionally, the peak density parameter (Sds) associated with waviness exhibited lower values for the LRM2 samples compared to the others. This indicates a reduced density of waviness peaks per unit area on the surfaces of the LRM2 samples.

The remelting treatments also impacted the geometry of the surface features. The values of Sdq and Ssc related to waviness, displayed in Table 5, suggest that the treatment with lower energy input resulted in more inclined (Sdq_LRM1 > Sdq_AB) and sharper (Ssc_LRM1 > Ssc_AB) peaks and valleys. Conversely, the treatment with higher energy input spread the material more evenly, resulting in a much lower curvature of the peaks compared to the AB samples (Ssc_LRM2 < Ssc_AB).

It should be noted that the asperity curvature (Ssc), root mean square slope (Sdq) and peak density (Sds) measured on the waviness profiles (Table 5) were much lower than the values measured on the primitive surfaces (Table 4), because these parameters were disproportionately affected by the fine-scale roughness and indeed were similar to those measured on the filtered roughness surfaces (Table 5).

It is also interesting to note that the decrease in waviness amplitude produced by the more energetic remelting treatment (LRM2) was

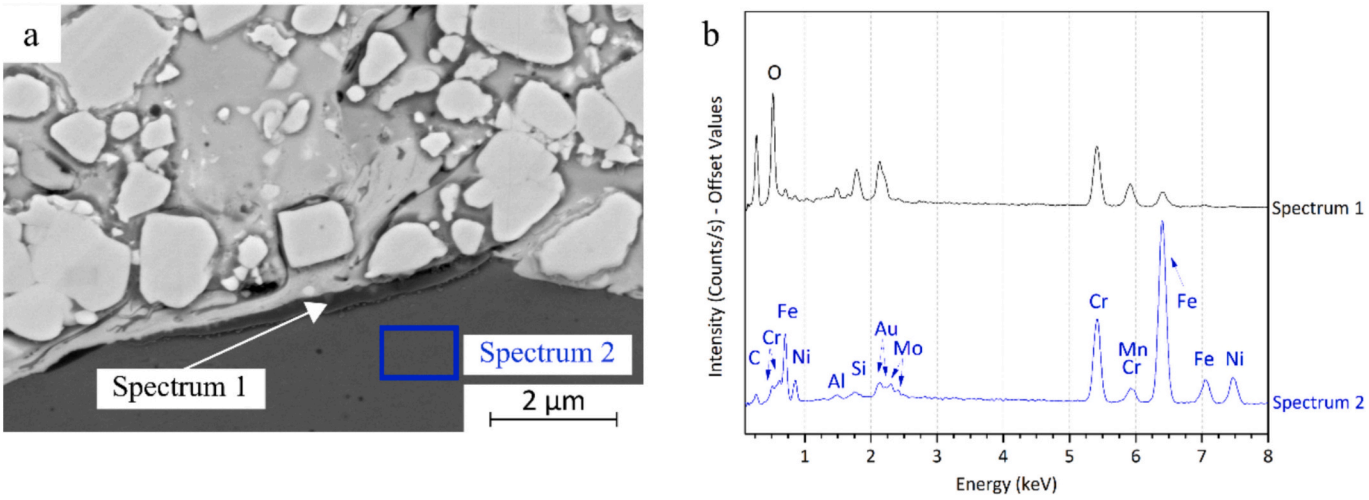

Fig. 13. SEM micrography (backscattered electrons) of the cross-sections of the coating-substrate interface in the AB sample (a), with corresponding EDX spectra (b).

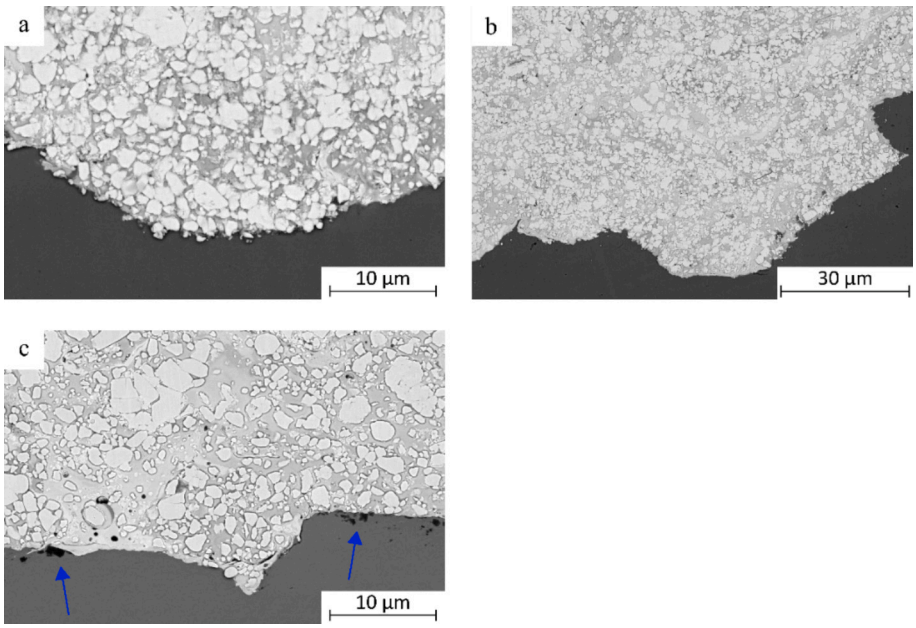

Fig. 14. SEM micrographs (backscattered electrons) showing details of the coating-substrate interface in the LRM2_P sample (a), P sample (b), and W sample (c). Blue arrows = grit inclusions.

accompanied by a proportionally even greater decrease in the average amplitude (Sa, Sq) and slope (Sdq) of the fine-scale roughness (Table 5). At the same time the height distribution of the filtered roughness profile became slightly negatively skewed (Ssk < 0) after the LRM2 treatment, because dales became the largest feature (Svk > Sk, Spk). These changes reflected quantitatively the more efficient melting of the adhered powder particles, as noted previously. These indeed contributed to the amplitude of the fine-scale roughness within each laser track.

After the deposition of the coatings, all the samples exhibited a very similar surface morphology, irrespective of whether the substrate was produced via L-PBF or traditionally made, and regardless of the surface conditions, as shown by the 3D reconstructions in Fig. 5. The pattern resulting from the laser passes, visible on the substrates' surfaces (Fig. 3), was no longer detectable on the coated samples.

Similarly, the roughness values calculated for the various L-PBF samples were quite consistent with each other and only marginally higher than those calculated for the reference samples (Table 6). The roughness amplitude (Sa, Sq, Sz) of the coatings (Table 6) was lower than that of the substrates (Table 4). These results highlight that the coating had the capability to level the underlying surface, hiding its morphological features, as also visible by the cross-sectional micrographs in Fig. 6, and consistent with our previous findings [34].

3.2. Coatings' microstructure, phase composition, and micro-mechanical properties

Homogeneous coatings, between 220 and 280 µm thick (Fig. 7), were obtained on all substrates, whether manufactured by L-PBF or produced traditionally (Fig. 8). With the exception of some minor porosity mostly located next to the surface of the coatings, the deposited material layer appeared dense and homogeneous, when viewed at low magnification, even where the substrates presented significant protrusions or alterations in surface morphology (see the red arrows in Fig. 8), likely due to the presence of semi-molten particles attached to the L-PBF surfaces following the building process, as noted previously (Section 3.1). These protrusions were indeed observed on the as-built substrates or on those

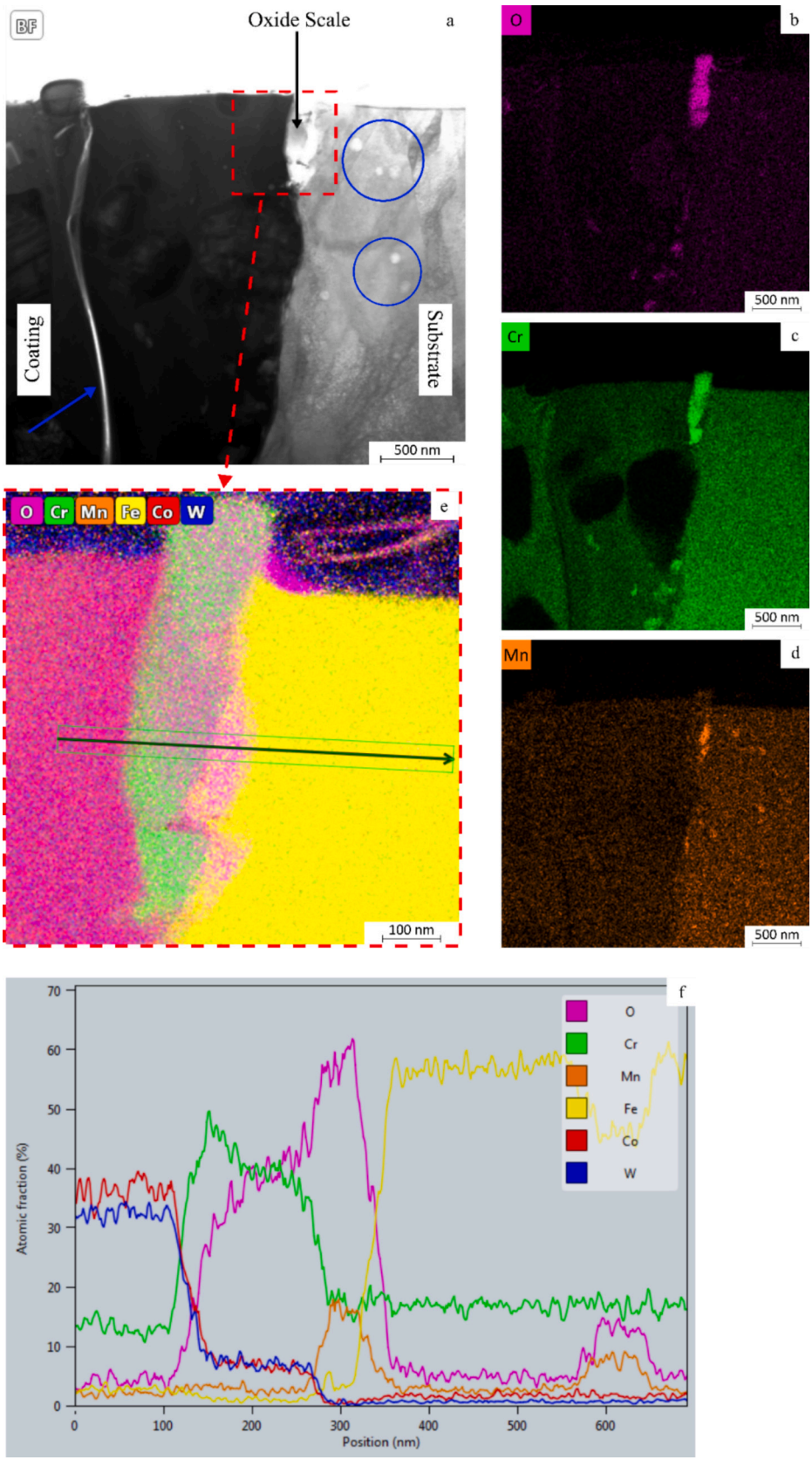

Fig. 15. TEM analysis of the coating-substrate interface in the AB sample: (a) bright-field view of the slice, (b, c, d) EDX maps of O, Cr, and Mn related to panel (a), (e) HAADF details of the area marked by the red dashed square in panel (a) with superimposed EDX maps, and (f) the corresponding EDX linescan along the direction marked in the panel above.

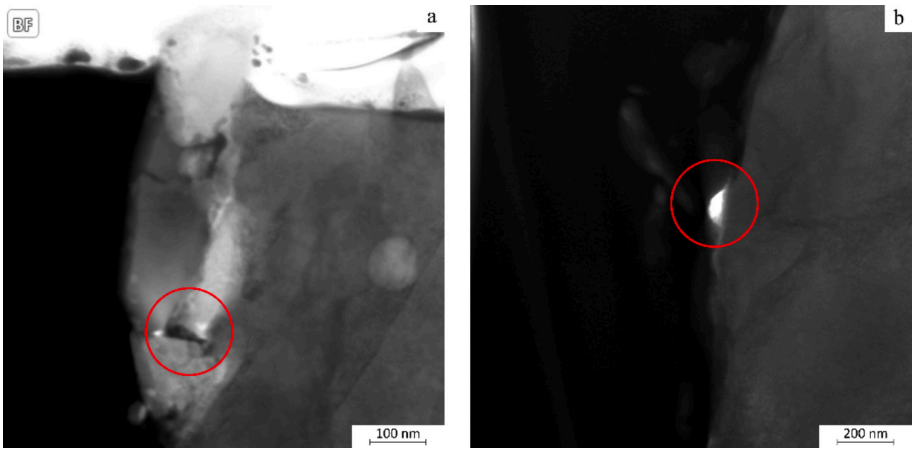

Fig. 16. TEM view of the coating-substrate interface in the AB sample: (a) bright-field view of the oxide flake at high magnification, (b) bright-field view of a different area of the coating-substrate interface. Red circles indicate defects.

subjected to the laser remelting process having a lower energy input (LRM1).

As also suggested by the optical profilometry acquisitions (see Section 3.1), regardless of surface morphology and roughness, the coating effectively covered each substrate. This reveals that the particles penetrated efficiently the surface dips thanks to the high kinetic energy with which they impacted the substrate.

The homogeneity of the deposited coatings was also confirmed by the results of the micro-mechanical tests. Considering the error range associated with the measurements, all coatings exhibited comparable properties. The average hardness value for the analysed coatings ranged between 13.3 and 14.4 GPa, while the average elastic modulus value varied from about 220 to 280 GPa (Table 7), aligning with the literature [46,47].

These findings indicate that the modifications made to the surface of L-PBF substrates by laser remelting did not affect the micromechanical properties of the coatings. Any potential alterations would probably be limited to areas located very close to the substrate surface, where the irregularity of the profile could impact the results. However, such alterations cannot be detected with this test.

The SEM micrographs in Fig. 9 provide a more detailed view of the coatings' microstructure. Some porosities were visible in the high-magnification micrographs (Fig. 9b, c, d), particularly near the boundaries between different splats (highlighted by the red dashed lines), as indicated by the red arrow in Fig. 9b. During the coating deposition process, phenomena of decarburization and dissolution of carbide particles occurred, changing the edges of some carbide particles from angular to rounded (blue arrows in Fig. 9d). The metal matrix exhibited a brighter contrast in backscattered electrons imaging mode in areas where these phenomena were more pronounced, as also observed in [46]. Interestingly, some carbide particles (highlighted by the blue circle Fig. 9d) appeared to be surrounded by a layer of brighter material, providing an instant picture of the decarburization processes they were undergoing during spraying.

High-magnification views also revealed that some localized defects were indeed present around the protrusions on the substrate surfaces (Fig. 10). They resulted from “shadow effects” caused by unmelted particles protruding from the substrate surfaces, but they were too small to be visible in the low-magnification views of Fig. 8.

Consistent crystalline phases were identified by XRD analyses in all deposited coatings, irrespective of the substrate conditions. Thus, Fig. 11 presents a single XRD pattern for the coatings, common to all samples. The pattern exhibited diffraction peaks corresponding to both WC and M_6C phases, similar to those detected in the feedstock powder. However, the M_6C peaks in the coating pattern have lower intensity compared to the powder one. The main secondary peaks in the coating pattern belong to the decarburized W_2C phase, which likely coincided with the brighter rim seen around some WC particles in Fig. 9 as discussed previously. The formation of this phase is a typical phenomenon that occurs during the thermal spray deposition of WC-Co-based materials [47,48]. Additionally, the shoulder in the W_2C peak near $2\theta = 40°$ suggests the presence of small amounts of metallic W.

3.3. Coating-substrate interface analysis

A <1 μm-thick oxide scale located at the coating-substrate interface of not-pickled samples is shown in the cross-sectional SEM micrographs in Fig. 12. It is highly probable that this oxide was formed during the production of the samples via L-PBF. In fact, it exhibited not only a similar Raman spectrum (see Section 3.1) but also a similar chemical composition (Fig. 13) to the oxide observed both on the surface and inside the bulk material of the as-built samples in [34]. The thin oxide scale was observed on both as-built surfaces and laser remelted ones. This suggests that the laser remelting treatments did not influence the formation of surface oxides. Namely, since the remelting was done inside the build chamber, it is likely that the oxide layer existing in the as-built condition was disrupted by the laser remelting process, but another, identical scale was then re-developed during solidification and cooling. The micrograph of the AB sample at higher magnification highlights some small cracks developed within the oxide scale, indicating its inherent brittleness (see the red circles in Fig. 12 b). These cracks may potentially weaken the interface areas where the oxide has formed, as they could easily propagate due to external stresses.

Consistent with the results of the Raman spectroscopy analyses (see Section 3.1), the coating-substrate interface of the pickled samples, regardless of the remelting conditions, appeared free of oxides (Fig. 14 a, b).

The wrought samples used as references showed the presence of some grit-blasting residues near the surface of the substrate (Fig. 14 c). This is expected due to the relative softness of the AISI 316 L stainless steel, into which residues from the impacting grit particles were embedded.

To better characterize the oxide scale on the coating-substrate interface, thin slices were extracted from an as-built sample and a pickled one and analysed by TEM. The main results are depicted in Figs. 15 and 17, respectively.

At the coating-substrate interface of the AB sample, an oxide flake is visible (Fig. 15a). The oxide is rich in Mn and Cr, as depicted in the EDX maps in Fig. 15 b, c, d. Interestingly, the maps suggest that the portion of the oxide scale rich in Mn was closer to the substrate, while the remaining portion, richer in Cr, was closer to the coating. Since the metal matrix of the coating consists of Co and Cr, it cannot be excluded

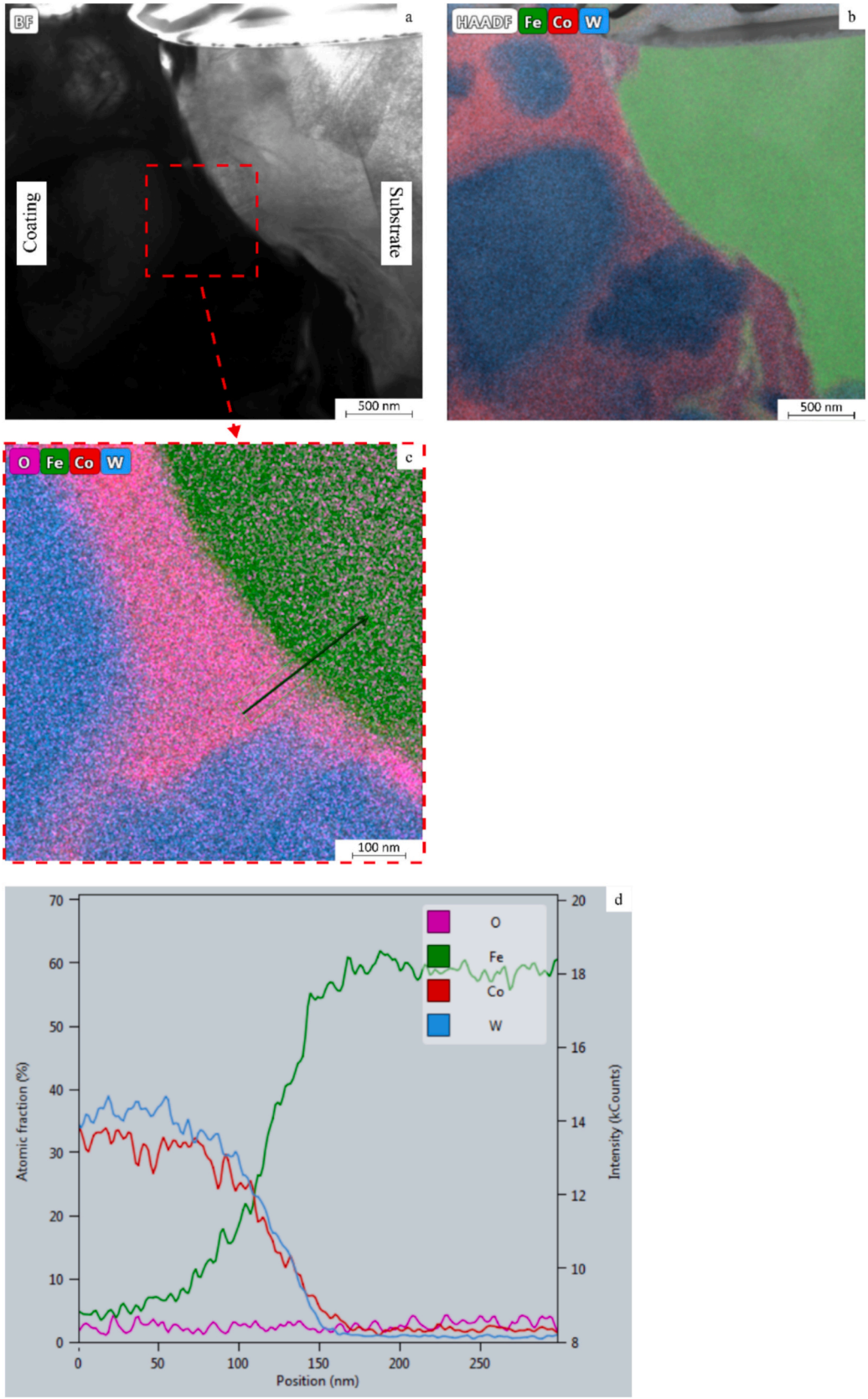

Fig. 17. TEM analysis of the coating-substrate interface in the P sample: (a) bright-field view of the slice, (b) EDX map showing the distribution of Fe, Co, and W relative to panel (a), (c) HAADF details of the area marked by the red dashed square in panel (a) with superimposed EDX maps, and (d) the corresponding EDX linescan along the direction marked in the panel above.

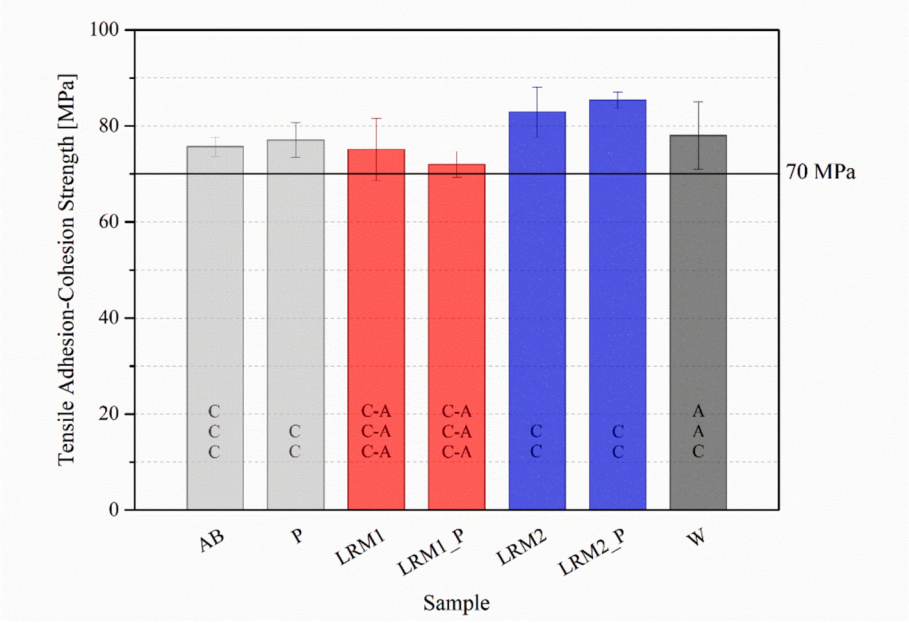

Fig. 18. Results of tensile adhesion tests on the coatings sprayed onto the L-PBF samples. Failure modes in each test are listed on the bars: "A" = adhesive failure, "C" = cohesive failure.

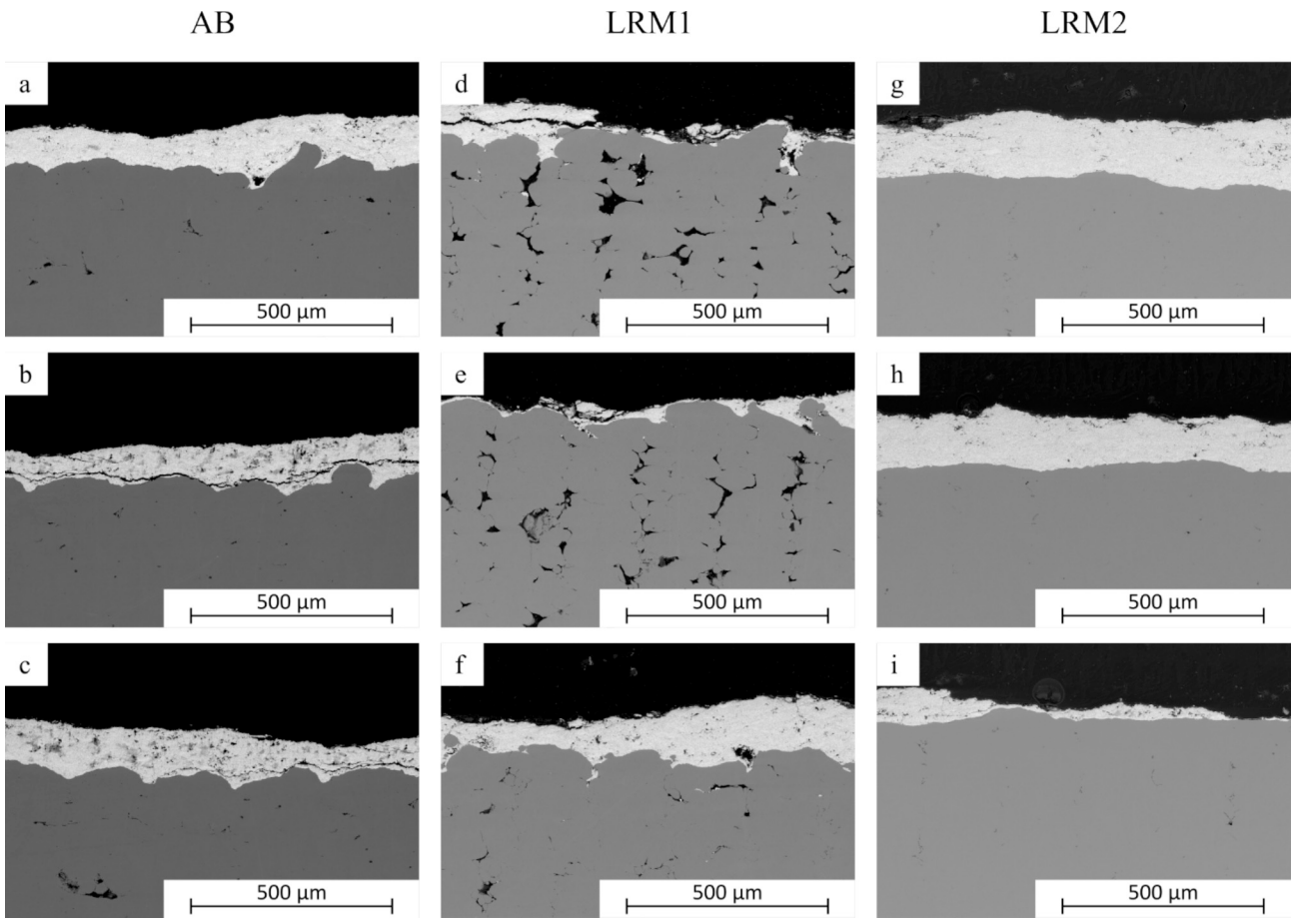

Fig. 19. Cross-sectional SEM micrographs of the coatings deposited onto L-PBF samples in (a, b, c) as-built (d, e, f) LRM1, and (g, h, i) LRM2 conditions, after tensile adhesion tests.

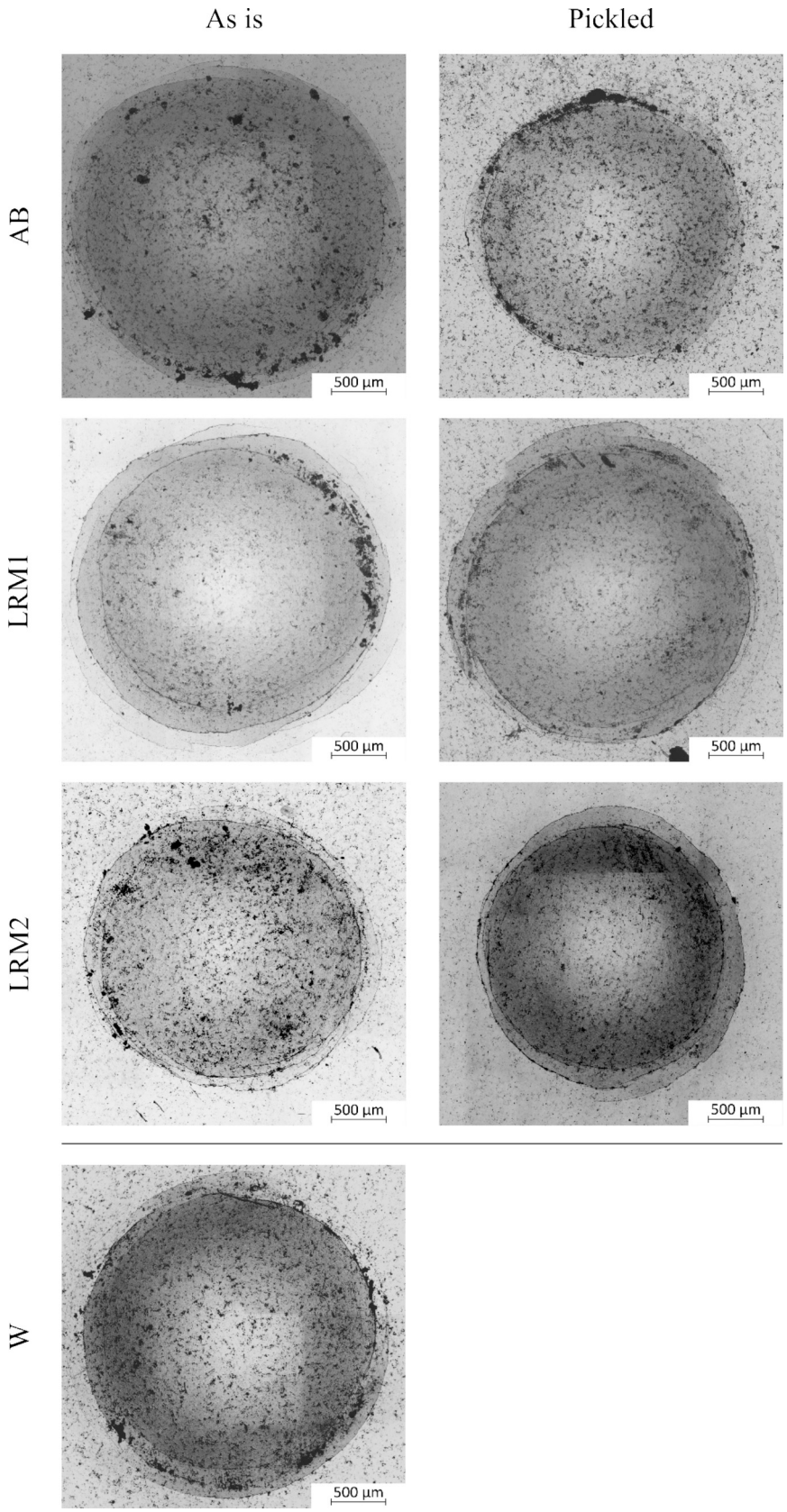

Fig. 20. Optical micrographs of cyclic impact marks on the polished top surfaces of HVOF-sprayed coatings deposited onto the samples in all conditions.

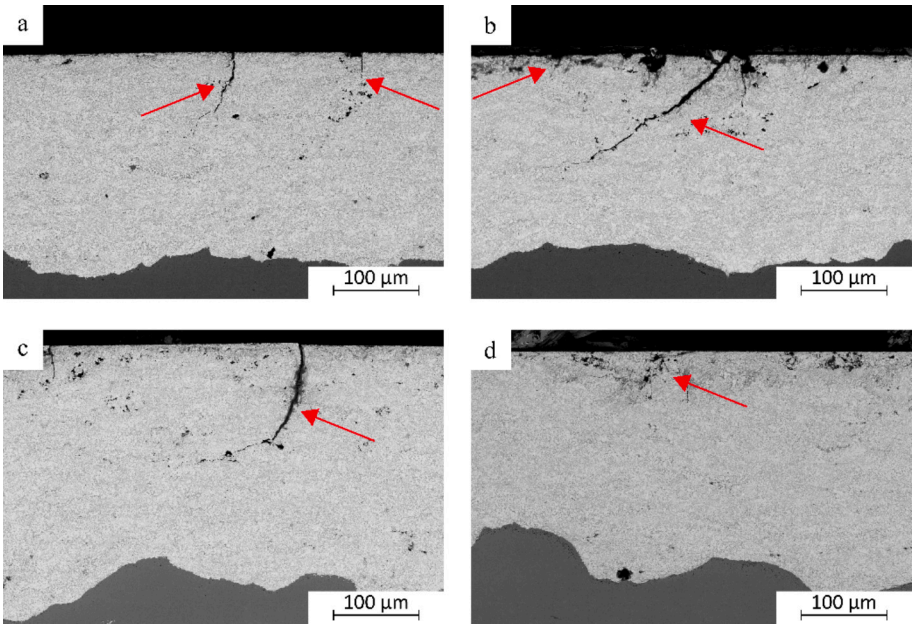

Fig. 21. Cross-sectional SEM micrographs (backscattered electrons) of the coatings deposited onto (a) AB, (b) P, (c) LRM1, and (d) LRM2_P samples, after cyclic impact testing. Red arrows indicate circumferential cracks propagating from the surface.

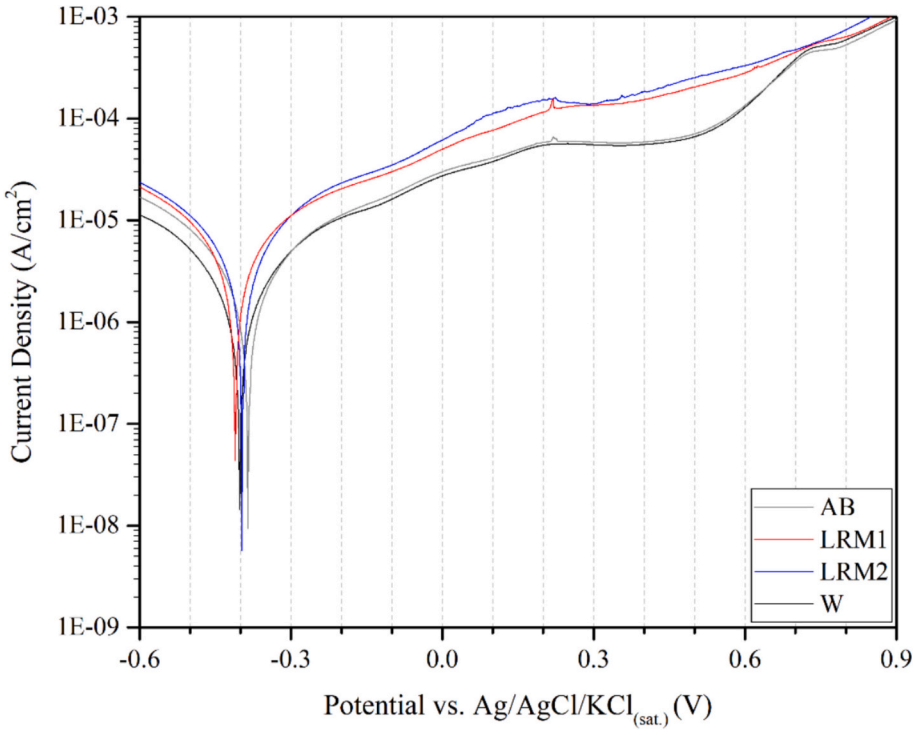

Fig. 22. Polarization curves of samples with different substrate surface conditions subjected to electrochemical polarization testing in 3.5 *w/v*% NaCl aqueous solution.

that the oxide formed at the interface was not solely originated from the oxidation of the substrate but could also be partly the result of the oxidation of the metal matrix of the coating. This is supported by the presence of small portions of material with high concentrations of oxygen and chromium within the coating itself (Fig. 15 b, c). During the deposition of the HVOF coatings, it is indeed possible that the powder experienced oxidation phenomena, despite the reduced heat input compared to other thermal spraying techniques [49]. On the other hand, dots of manganese-rich oxide were clearly visible within the substrate (Fig. 15 b, d), in the areas highlighted by the blue circles in Fig. 15 a. Therefore, the substrate appeared to contain small portions of oxide having a chemical composition similar to that of the bottom part of the oxide scale present at the interface with the coating. This observation aligns with the findings from the SEM-EDX analyses conducted during our previous study [34] and corroborates the idea that the oxide scale located at the interface with the coating originated during the L-PBF process.

Notably, in Fig. 15 a, a defect located along the boundary of a splat

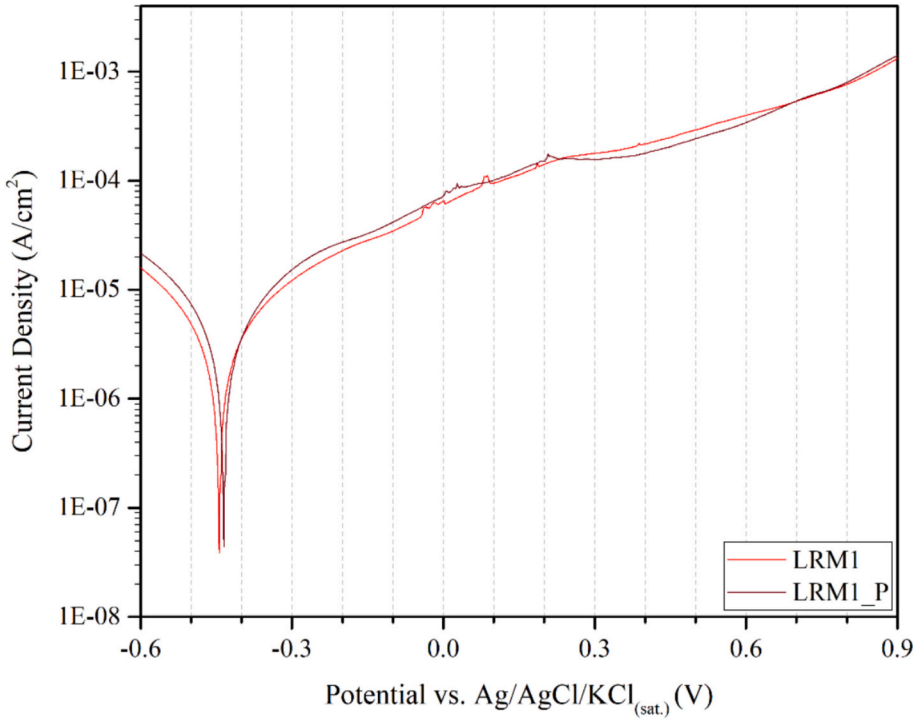

Fig. 23. Polarization curves of laser remelted samples as is (LRM1) and pickled (LRM1_P), subjected to electrochemical polarization testing in 3.5 w/v% NaCl aqueous solution.

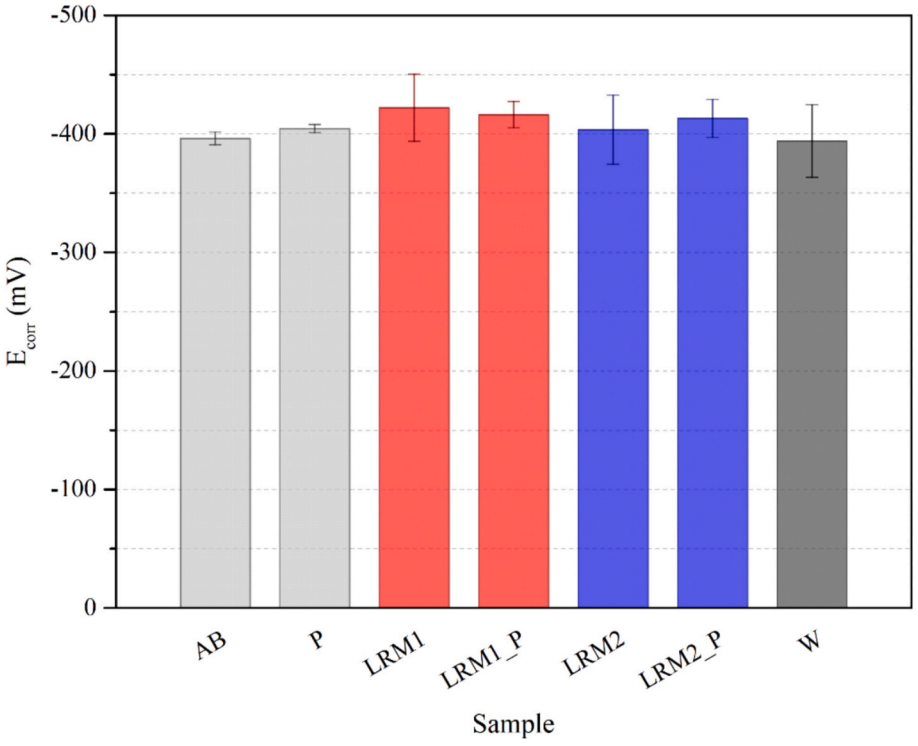

Fig. 24. Corrosion potential (E_{corr}) of samples subjected to electrochemical polarization testing in 3.5 w/v% NaCl aqueous solution.

was clearly visible within the coating, appearing as a bright line (as indicated by the blue arrow) due to its higher electron transparency. Therefore, it is possible that some elongated, narrow porosities formed between different lamellae of the coating, due to imperfect cohesion of the lamellae themselves. These defects could represent weaknesses in the coating or serve as preferential paths for the progression of corrosion phenomena, if reached by corrosive agents.

Additionally, defects were observed both in the oxide flake and at different locations along the coating-substrate interface, as indicated by the red circles in Fig. 16.

Different from the AB sample, the coating-substrate interface of the pickled sample (Fig. 17 a) appeared completely clean, without any

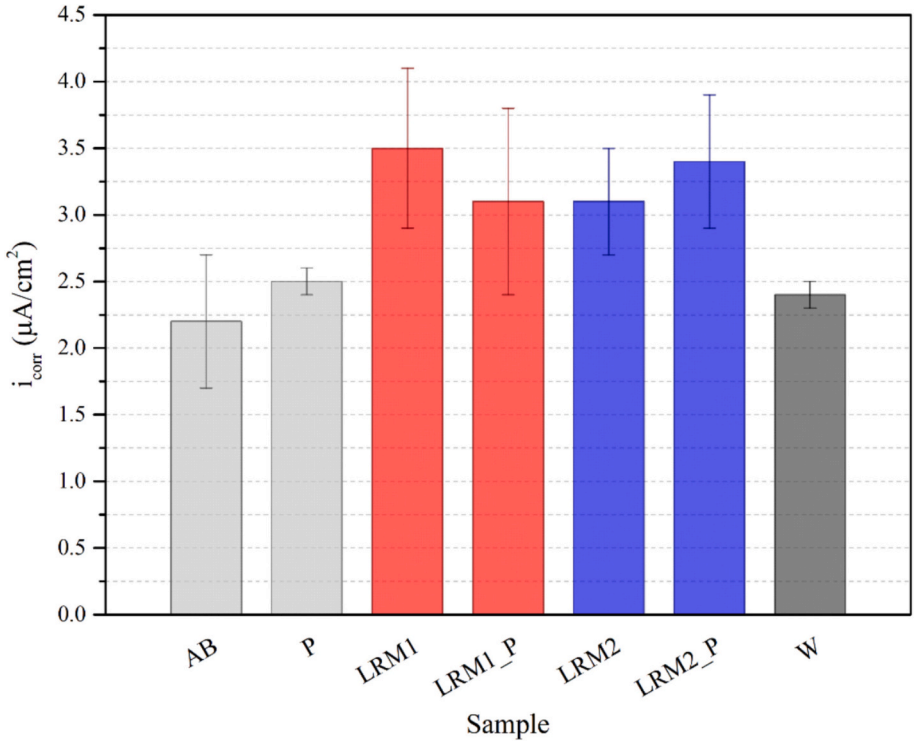

Fig. 25. Corrosion current density (i_{corr}) of samples subjected to electrochemical polarization testing in 3.5 w/v% NaCl aqueous solution.

detectable oxide scale or defect. The EDX maps (Fig. 17 b, c) and line-scans (Fig. 17 d) showed that Fe diffused from the substrate into the coating. In fact, along the linescan from the coating toward the substrate, the signal of Fe started to increase within the coating before the signals of Co and W started to decrease, indicating that Fe was indeed present within the coating, next to the substrate. The oxygen signal was constant at a very low value along all the line, confirming that no oxide flakes were present at the interface.

3.4. Coating-substrate adhesion

The results from the tensile adhesion tests indicated that, in general, all the coatings deposited in this study, regardless of the substrates' conditions, achieved adhesion values exceeding 70 MPa (Fig. 18). These values were comparable to those obtained in our previous study with similar coatings deposited on both L-PBF substrates (obtained under different conditions than the present ones) and wrought AISI304 substrates [34]. This confirms the good adhesion of the HVOF-sprayed WC-CoCr coatings to substrates produced using additive laser-based powder bed technologies.

Regardless of the substrates' surface conditions, the samples mainly exhibited cohesive failure. This contrasted with the result we obtained in [34], where as-built surfaces mainly led to adhesive failure phenomena. This result could be attributed to two possible causes. Firstly, as revealed by TEM analyses, the coatings deposited onto the AB samples exhibited some narrow yet relatively extensive defects along certain boundaries between splats. Therefore, it is possible that the presence of these defects partially affected the cohesion of the coating, which turned out to be lower than its adhesion to the substrate, despite the presence of thin surface oxide scales. In other words, it seems that the presence of a surface oxide scale did not sufficiently weaken the interface with the substrate to induce a primarily adhesive failure, because of the presence of some defects between the coating's splats. This corroborates the hypothesis made in [34] that the adhesion of the coatings to L-PBF substrates on which an oxide scale was present was only slightly lower than their internal cohesion.

Secondly, it is possible that the oxide scale present on the samples obtained in this work was so thin and discontinuous that it did not affect the adhesion between the substrate and the coating at all.

The samples treated with the less energetic laser remelting treatment (LRM1 and LRM1_P) were the only ones that exhibited a mixed cohesive-adhesive failure mechanism, with signs of adhesive fracture in certain areas of the surface (label “C-A" in Fig. 18). Since this effect was observed regardless of whether the samples had undergone pickling or not, it is possible that the morphological modifications induced by the treatment on the surface of these samples weakened the mechanical adhesion of the coating in certain surface areas, thereby reducing the adhesive strength of the coating to the substrate. The roughness amplitude (Sa, Sq) of the LRM1 substrates was only slightly higher than that of the LRM2 substrates (Table 5); therefore, the morphology of the surface asperities and valleys, as well as their distribution on the surface, arguably played a more critical role in influencing the adhesion failure mechanism. As described in Section 3.1, the LRM1 samples, whether pickled or not, were the ones that exhibited notably more inclined, sharper asperities and valleys compared to both the AB and LRM2 samples. These morphological features may have affected coating adhesion, potentially inhibiting the proper adhesion of some splats.

On the contrary, samples treated with laser remelting at higher energy input (LRM2) exhibited greater cohesive strength compared to the other samples.

The main differences between the LRM2 surfaces and the others were related to the density of peaks (see Sds values in Table 5) and the presence of less inclined and curved features (Table 5). These features could have contributed to a different stress distribution within the coating material, reducing stress concentrations near sharp geometrical irregularities induced by the substrate profile and ultimately enhancing its internal cohesion. Indeed, the rough profiles of the L-PBF samples and the combination of materials with different elastic moduli could have generated stress peaks, which likely discharged into the coating immediately above the interface. The stress distribution probably varied with the substrate profile following the remelting treatment, potentially contributing to the observed superior tensile adhesion-cohesion

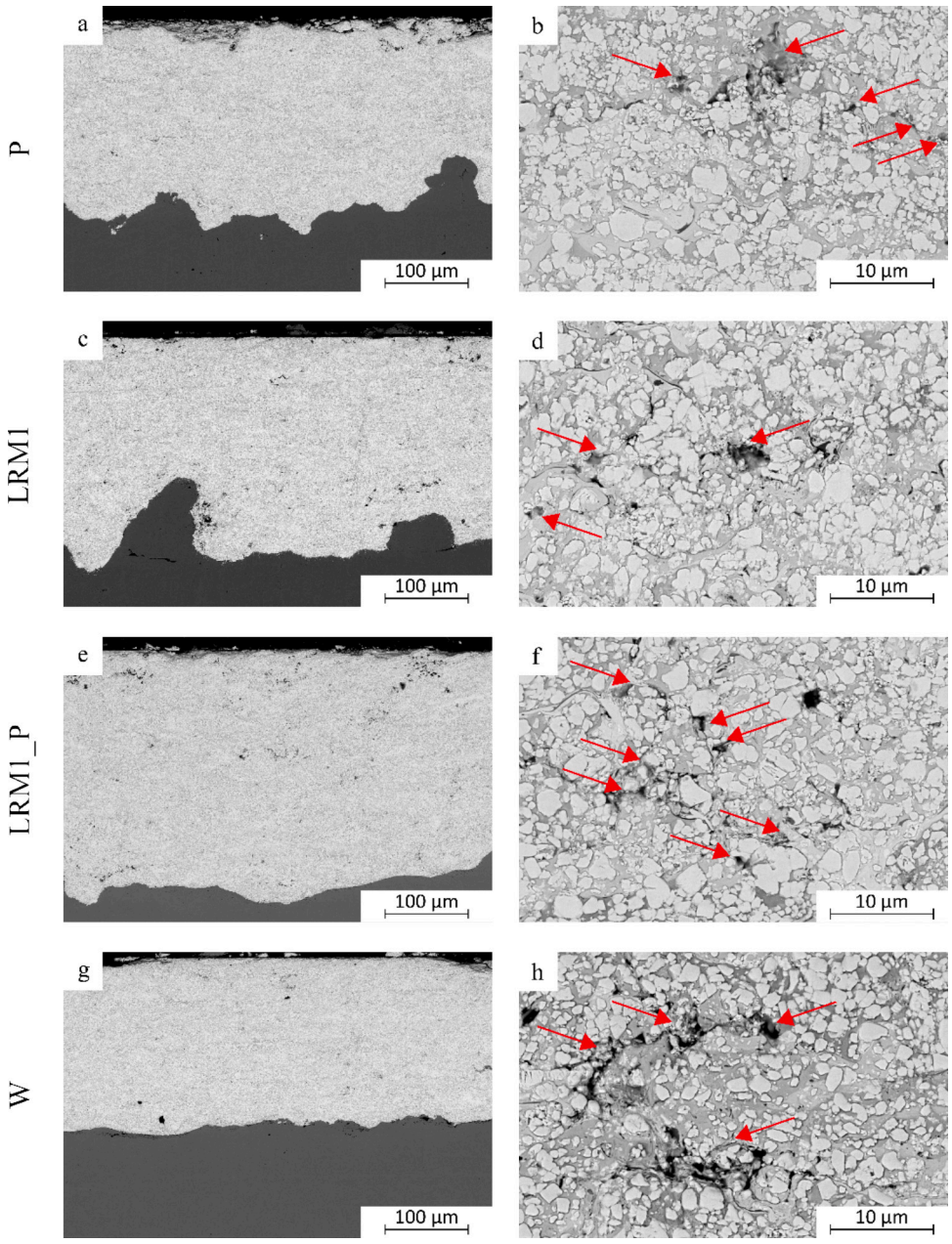

Fig. 26. Cross-sectional SEM micrographs of the coatings deposited onto L-PBF samples in (a, b) as-built and pickled conditions, (c, d) LRM1 conditions, (e, f) LRM1 and pickled conditions, and on wrought samples (g, h), after polarization tests. The arrows indicate signs of internal corrosion in the coating.

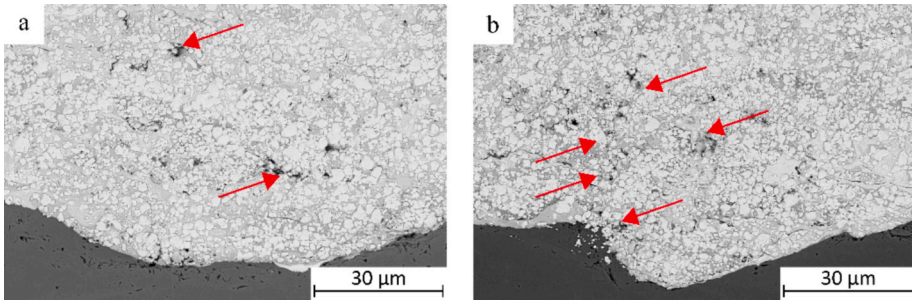

Fig. 27. Cross-sectional SEM micrographs of the coatings deposited onto an LRM1_P sample (a) and an LRM2 sample (b) next to the interface with the substrates. The arrows indicate signs of internal corrosion in the coating.

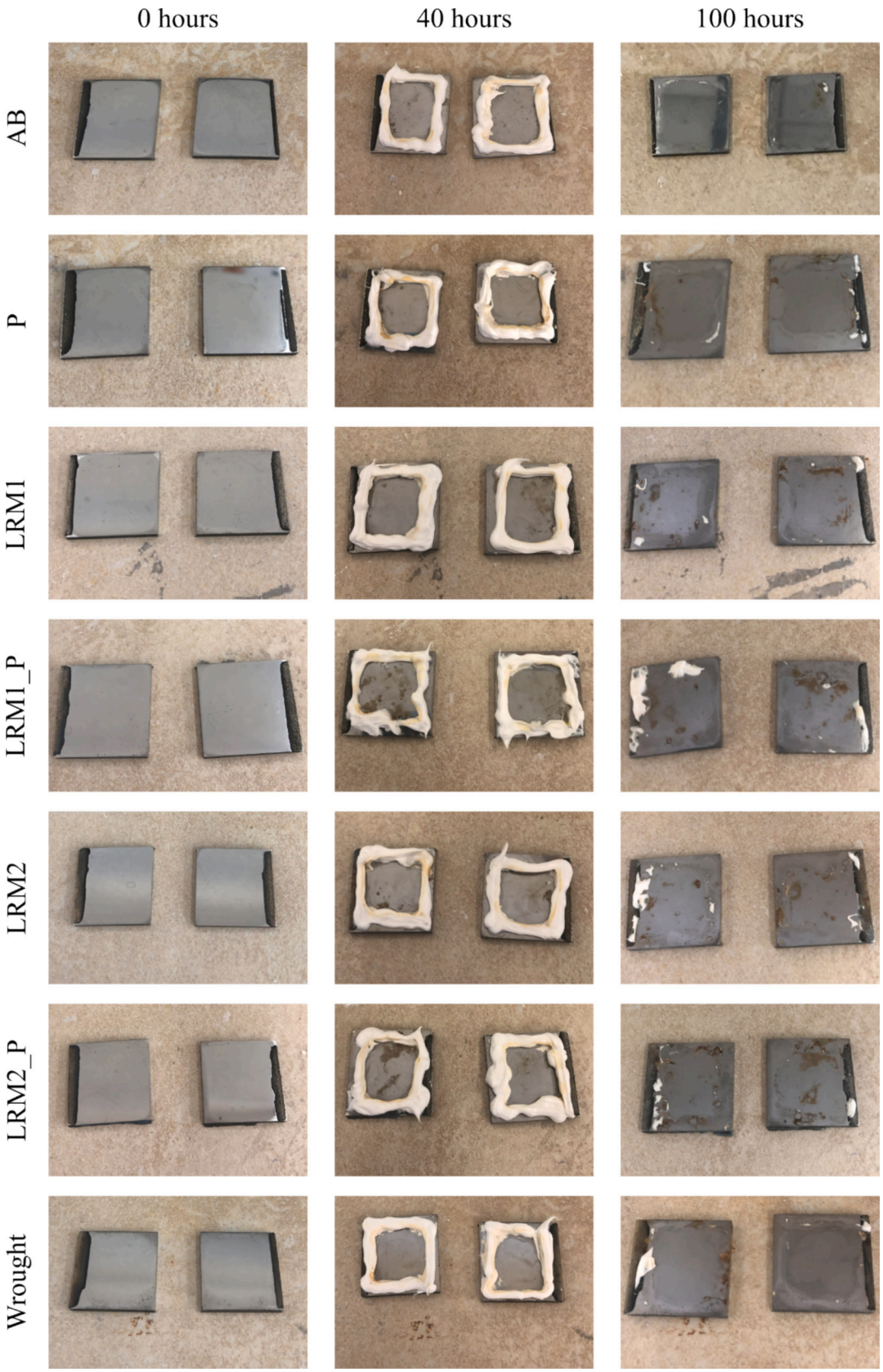

Fig. 28. Photographs of the samples subjected to the corrodkote test: at the beginning of the test, after 40 h, and after 100 h.

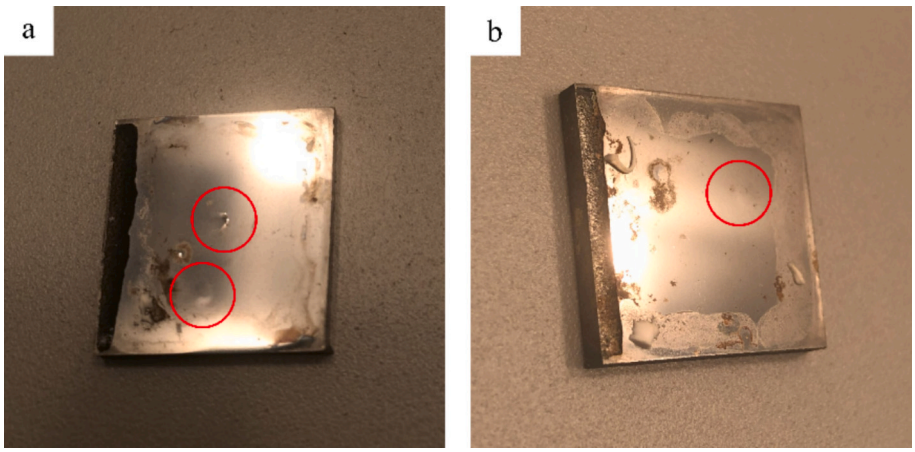

Fig. 29. Photographs of samples subjected to the corrodkote test after 100 h: a) AB and b) LRM1. Red circles indicate swelling of the coating.

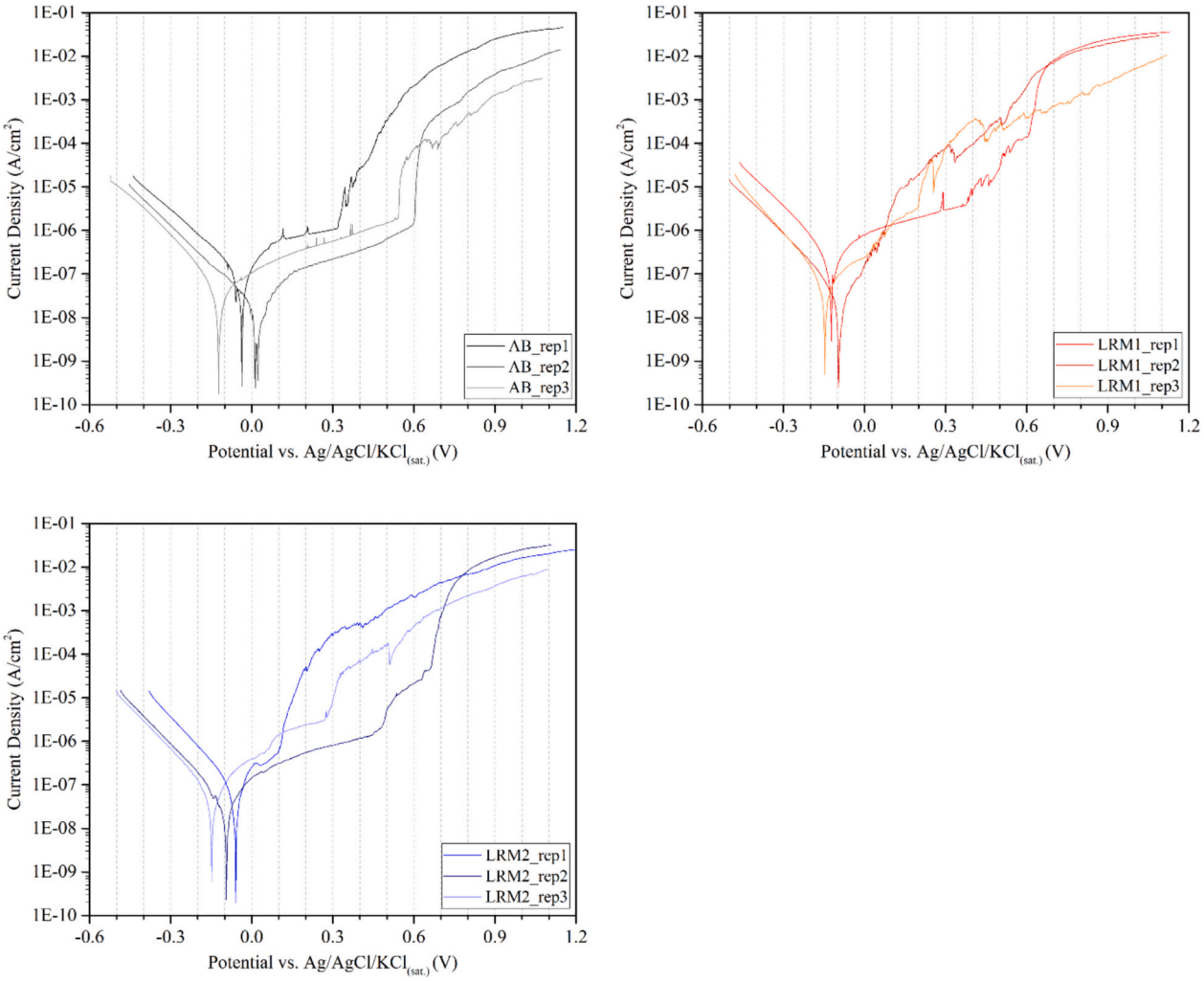

Fig. 30. Comparison between the polarization curves obtained from different repetitions of the electrochemical polarization test on uncoated AB, LRM1, and LRM2 substrates in 3.5 w/v% NaCl aqueous solution.

strength.

The SEM analyses performed on the cross-sections of selected samples after the tensile adhesion tests supported the hypothesis of different stress distributions in the coatings deposited on laser remelted substrates. Indeed, as shown in the SEM micrographs in Fig. 19, coating failure occurred at different distances from the interface. In details, the average remaining coating thickness was about 90 μm for the AB samples and 120 μm for the LRM2 samples. In both cases, failure mainly occurred at similar distances from the interface, with a few localized exceptions (see Fig. 19 h). On the other hand, the LRM1 samples exhibited more varied failure locations, with some areas showing only a few microns of coating still attached to the substrates, while other areas

maintained >100 μm of coating. In other words, it seems that failure in the LRM1 samples was more inhomogeneous compared to the other specimens.

Even after the impact tests, failure was of a purely cohesive type. Specifically, cohesive failure within the coatings became visible in the form of circumferential cracks along the boundary of the impact marks obtained on the surfaces of the samples (Fig. 20). Interestingly, no radial cracks were observed, indicating that aside from the breakthrough caused by bending of the coating during the impacts of the sphere, no other failures occurred in the coatings. As also observed in [34], cross-sectional SEM analysis of the impact marks revealed that, consistent with the findings from finite element calculations in [50], certain cracks propagated from the surface across the coating at an off-normal angle with respect to the polished surface, as indicated by the arrows in Fig. 21. The main difference observed between these samples and those tested in [34] was that, in the present study, the cracks caused by the impacts propagated within the coating without reaching the interface with the substrate (Fig. 21) and without propagating along the coating-substrate interface even in the as-built samples. This difference with [34], where the as-built samples exhibited a slightly thicker and more continuous oxide coverage that resulted in a few circumferential cracks eventually propagating along the interface, means that the thickness and coverage of the oxide scale on the as-built samples affects the adhesion of the coating.

Regarding the laser remelting treatment effects, the observations indicated that qualitatively, there were no noticeable differences in the behaviour of the samples subjected to laser remelting compared to those that were not. The difference in tensile adhesion strength between the LRM1 and LRM2 samples was likely too small to produce qualitatively perceivable differences in the impact test.

3.5. Corrosion behaviour of the samples

After the electrochemical polarization tests, the shape of the polarization curves did not show variations dependent on either the laser remelting treatment (Fig. 22) or the pickling treatment (Fig. 23). Therefore, the corrosive phenomena that occurred during the test were unaffected by the substrate conditions. The coatings exhibited similar behaviour when subjected to corrosion in a saline environment, and consistently, the corrosion potential values (E_{corr}) calculated for the different samples were similar to each other, ranging between −375 mV and − 425 mV (Fig. 24). This result was expected, as the chemical composition and deposition parameters of the coatings were constant across all samples. The obtained values align with those reported in the literature for these coatings [51].

However, some differences emerged concerning the corrosion current density (i_{corr}), as depicted in Fig. 25. The measured i_{corr} values fell within a range varying between ≈ 2.0 and 3.5 μA/cm^2. These values are generally comparable to those reported in the literature [51–53]. Nonetheless, the samples subjected to laser remelting exhibited higher average i_{corr} values than the as-built or wrought samples (Fig. 25). Their polarization curves were indeed shifted to slightly higher current density values (Fig. 22). This suggests that the corrosive phenomena progressed slightly faster in the samples subjected to laser remelting compared to the others.

SEM analyses revealed some microscopic signs of corrosion localized near the surface of some samples, as displayed in Fig. 26 a. At higher magnification, the effects of the corrosion progression were observed in all tested samples. Corrosion mainly affected the metal matrix of the coatings, which is a phenomenon typically found in HVOF WC-based cermet coatings exposed to saline environments [51,54].

As indicated by the red arrows in Fig. 26, corrosion proceeded along preferential paths outlined by interlamellar defects, allowing corrosive agents to penetrate from the surface of the sample deep into the coating. It is possible that corrosion proceeded more rapidly where these defects were more concentrated. Occasionally, these paths allowed corrosive agents to reach the interface with the steel substrate (Fig. 27). However, even when this occurred, no corrosion products originating from the substrate were observed at the interface, indicating that the substrate was apparently unaffected by corrosion phenomena. Therefore, it is probable that the corrosive species reaching the substrate were present in minimal quantities, insufficient to induce corrosion of the stainless steel.

Some differences in the corrosion behaviour of the samples also emerged after the corrodkote test. The as-built samples, whether pickled or not, and the wrought reference samples did not exhibit evident signs of corrosion after 40 h (i.e. 2 cycles) of testing, as shown in Fig. 28. It is important to highlight that the area of interest for evaluating the progression of corrosion phenomena is within the silicone boundary. The area beneath the silicone, in fact, experienced different conditions compared to the area of interest and should not be considered when evaluating the samples' behaviour. The surfaces of the as-built and wrought samples maintained a metallic shine and were free of visible pits or reddish deposits typically associated with substrate corrosion. The similar behaviour of these samples mirrored the findings from the electrochemical polarization tests, during which both the as-built and the reference samples exhibited no noticeable differences. These outcomes confirm that HVOF WC-CoCr coatings can be deposited on both traditional and L-PBF substrates without compromising the corrosion performance of the coatings themselves. At the end of the test, however, the as-built samples not subjected to pickling exhibited some small signs of swelling. To see this more clearly, larger images of some of the same samples shown in Fig. 28 are provided in Fig. 29, with swelled blisters indicated by red circles. This was the result of the corrosion of the substrate and the subsequent accumulation of corrosion products at the interface with the coating [55]. This difference between as-built and pickled samples can be interpreted by assuming that, when corrosive agents penetrated across interconnected defects and came in contact with area of the substrate surface covered by the thin oxide scale noted in Section 3.2, they could spread through the microcracks sometimes seen in the scale itself (Fig. 12) and affect a larger portion of the interface. By contrast, the tighter interface provided by the pickled substrate, where interdiffusion between the coating and the substrate itself was seen (Fig. 17 and Section 3.3), limited the spread of the corrosive agents along the interface. Therefore, even when corrosive agents could penetrate down to the substrate, they could not affect an area large enough to accumulate a substantial amount of corrosion products and swell the coating.

In contrast, the samples subjected to laser remelting, regardless of the treatment parameters, exhibited surface corrosion signs after 40 h of treatment (Fig. 28). In detail, these samples showed reddish deposits on the surface, typically associated with corrosion of the ferrous substrate. This behaviour can again be explained by assuming that corrosive agents penetrated down to the substrate where defects within the coating provided a continuous path for corrosive agents from the surface to the substrate interface. The inferior performance exhibited by the samples subjected to laser remelting aligns with the results of the electrochemical polarization tests, during which these samples displayed higher corrosion current density values compared to the others.

It can be deduced that either the topography of the laser-remelted substrates promoted the presence of a few more localized internal defects in the coating that helped the progression of corrosion, acting as preferential paths for the advance of corrosive agents, or that the remelting process affected the corrosion resistance of the stainless-steel substrate itself, so that it corroded more rapidly when exposed to even a tiny amount of corrosive agents. The possibility that the remelting treatments affected the corrosion resistance of the substrate was investigated through electrochemical polarization tests conducted on uncoated samples. However, these tests did not conclusively determine whether substrate deterioration occurred after remelting. Indeed, as shown in Fig. 30, the polarization curves obtained from different repetitions of the tests did not perfectly overlap, indicating variability in the

responses within each sample. This might have been associated with localized defects (e.g. porosity) randomly distributed in the L-PBF samples. This inconsistency suggests that the material's behaviour could not be definitively characterized by these tests.

Nonetheless, it would look like there was more variability among the polarization curves obtained from the laser remelted samples. At least one curve each for the LRM1 and LRM2 samples showed almost no passivation of the uncoated stainless steel, while all curves acquired on the as-built surfaces exhibited a well-developed passive stage, although the passivity breakdown potential varied widely among the three curves (Fig. 30). However, other test repetitions on LRM1 and LRM2 samples did not consistently confirm the lack of passivation. Thus, the exact effects of the remelting treatments on the substrates remain unclear, and the causes of the increased corrosion currents observed in the coated LRM1 and LRM2 samples are yet to be fully understood.

However, even with the laser remelted samples the beneficial effect of pickling could be seen. Indeed, the coatings on the remelted samples not subjected to pickling exhibited some small signs of swelling, indicated by the red circles in Fig. 29 b, while the coatings on the remelted and pickled samples exhibited reddish spots but no swelling. Therefore, the same considerations made above concerning the relevance of pickling toward limiting the spread of corrosive agents along the coating-substrate interface apply.

The evidence of substrate corrosion observed during the corrodkote test, which was not detected by the SEM analyses of the coated samples subjected to electrochemical polarization tests, highlights the different conditions to which these two tests expose the samples. The corrodkote test is an accelerated test that subjects the samples to extremely harsh corrosion conditions. The samples are exposed to high humidity and concentrated corrosive agents (chlorine, ferric and cupric ions) for an extended period. Consequently, during this test the corrosive agents have more time to attack the substrate. This prolonged exposure creates conditions conducive to the development of corrosive phenomena that can be detrimental to the substrate itself, even if it is made of a typically corrosion-resistant material.

4. Conclusions

This work investigated the deposition of HVOF-thermally sprayed coatings on AISI 316 L laser powder bed fused (L-PBF) parts, using a WC-10%Co-4%Cr powder as feedstock material for the coating deposition. We focused on modifying the surface of the L-PBF substrates using in-situ laser remelting and pickling to evaluate how different substrate surface conditions could affect the adhesion and the corrosion performance of the coatings. Two laser remelting treatments with different energy densities were applied to the L-PBF surfaces at the end of the building process, within the building chamber. In the first treatment (LRM1) a laser power of 90 W and a scanning speed of 1500 mm/s were employed, while the second treatment (LRM2) used a laser power of 95 W and a scanning speed of 500 mm/s. The as-built and laser remelted substrates were coated both before and after a pickling treatment. As a reference, bulk stainless steel samples subjected to grit-blasting were employed. The main conclusions can be summarized as follows:

- Regardless of the substrates' surface conditions, the HVOF process produced dense and homogeneous coatings, with micro-mechanical properties that were not affected by the conditions of the substrate. Additionally, the coating deposition levelled the surface, hiding the morphological differences among the substrates.
- The laser remelting treatments modified the surface morphology of the L-PBF samples. In particular, the most energetic treatment resulted in a surface with more widely spaced grooves and melted most of the spherical particles attached to the surface, leading to a more uniform distribution of the material.
- After the tensile adhesion tests, all samples exhibited primarily cohesive failures, including the as-built samples, where thin oxide flakes were present at the interface between the substrate and the coating. This indicates that a discontinuous and thin oxide scale cannot significantly affect the adhesion of the coating to the substrate.

  The different substrate morphologies induced by the remelting treatments nonetheless impacted the test results, likely altering the stress distribution within the first layers of the coatings. Specifically, the LRM2 samples exhibited better performance, displaying an adhesion-cohesion strength exceeding 80 MPa, while all other samples showed values of about 70 MPa and, in the case of the LRM1 samples, some adhesive failure was also seen.
- The corrosion resistance of the coatings was slightly worsened by the laser remelting treatments of the substrates. In particular, substrate corrosion occurred in areas exposed to the corrosive agents that penetrated through internal defects in the coatings. This assumption was supported by the results of the corrodkote test, where reddish deposits were observed on the surface of the remelted samples. Because the microstructure of the coatings and their internal defects were the same in all cases, the different responses of the coated systems were probably due to differences in the corrosion resistance of the substrate. Electrochemical polarization tests on uncoated, laser-remelted substrates suggested more point-to-point variability with the possibility of areas having impaired passivation ability, but the results were not conclusive. Pickling, on the other hand, slightly improved the corrosion resistance regardless of the substrate condition.

The results of this work provided some interesting insights regarding the impact of the remelting treatments. Specifically, a laser remelting treatment, appropriately optimized, reduces the presence of semi-molten particles on the surface, reducing the shadow effects during the coating deposition. Additionally, it may be able to improve the adhesion-cohesion strength of the coatings, ensuring superior performances compared to those achievable with as-built substrates. Indeed, this work highlighted that the substrate surface morphology can influence both the type of failure, ranging from purely cohesive to cohesive-adhesive, and the internal cohesion strength of the coating. At the same time, further investigation should be conducted into the possible sensitization that these treatments could induce on L-PBF stainless-steel substrates.

CRediT authorship contribution statement

Maria Francesca Bonilauri: Writing – review & editing, Writing – original draft, Visualization, Methodology, Investigation, Formal analysis, Conceptualization. **Matteo Perini:** Writing – review & editing, Visualization, Supervision, Methodology, Investigation, Formal analysis, Conceptualization. **Sasan Amirabdollahian:** Writing – review & editing, Methodology, Investigation. **Laura Paglia:** Methodology, Investigation, Formal analysis. **Giovanni Pulci:** Supervision, Methodology. **Francesco Marra:** Supervision, Methodology. **Edoardo M. Rossi:** Methodology, Investigation, Formal analysis. **Luca Lusvarghi:** Supervision, Conceptualization. **Giovanni Bolelli:** Writing – review & editing, Supervision, Project administration, Methodology, Investigation, Formal analysis, Conceptualization.

Declaration of competing interest

The authors declare that they have no known competing financial interests or personal relationships that could have appeared to influence the work reported in this paper.

Data availability

Data will be made available on request.

References

[1] J.O. Milewski, Additive manufacturing metal, the art of the possible, in: Springer Series in materials Science, Springer Verlag, 2017, pp. 7–33, https://doi.org/10.1007/978-3-319-58205-4_2.

[2] I. Gibson, D. Rosen, B. Stucker, M. Khorasani, Introduction and basic principles, in: Additive Manufacturing Technologies, Springer, Cham, 2021, pp. 1–21, https://doi.org/10.1007/978-3-030-56127-7_1.

[3] T.D. Ngo, A. Kashani, G. Imbalzano, K.T.Q. Nguyen, D. Hui, Additive manufacturing (3D printing): a review of materials, methods, applications and challenges, Compos B Eng 143 (2018) 172–196, https://doi.org/10.1016/j.compositesb.2018.02.012.

[4] M. Srivastava, S. Rathee, V. Patel, A. Kumar, P.G. Koppad, A review of various materials for additive manufacturing: recent trends and processing issues, J. Mater. Res. Technol. 21 (2022) 2612–2641, https://doi.org/10.1016/J.JMRT.2022.10.015.

[5] D. Bourell, J.P. Kruth, M. Leu, G. Levy, D. Rosen, A.M. Beese, A. Clare, Materials for additive manufacturing, CIRP Ann. 66 (2017) 659–681, https://doi.org/10.1016/J.CIRP.2017.05.009.

[6] A. Vafadar, F. Guzzomi, A. Rassau, K. Hayward, Advances in metal additive manufacturing: a review of common processes, Industrial Applications, and Current Challenges, Applied Sciences 11 (2021) 1213, https://doi.org/10.3390/APP11031213.

[7] I. Gibson, D. Rosen, B. Stucker, M. Khorasani, Powder Bed Fusion Additive Manufacturing Technologies, Springer, Cham, 2021, pp. 125–170, https://doi.org/10.1007/978-3-030-56127-7_5.

[8] N.D. Dejene, H.G. Lemu, Current status and challenges of powder bed fusion-based metal additive manufacturing: literature review, Metals 13 (2023) 424, https://doi.org/10.3390/met13020424.

[9] M. Leary, Powder bed fusion, in: Design for Additive Manufacturing, Elsevier, 2020, pp. 295–319, https://doi.org/10.1016/B978-0-12-816721-2.00011-7.

[10] M. Leary, Surface roughness optimisation for selective laser melting (SLM): Accommodating relevant and irrelevant surfaces, in: Laser additive manufacturing: materials, design, technologies, and applications, Elsevier Inc., 2017, pp. 99–118, https://doi.org/10.1016/B978-0-08-100433-3.00004-X.

[11] G. Strano, L. Hao, R.M. Everson, K.E. Evans, Surface roughness analysis, modelling and prediction in selective laser melting, J. Mater. Process. Technol. 213 (2013) 589–597, https://doi.org/10.1016/j.jmatprotec.2012.11.011.

[12] J.C. Snyder, K.A. Thole, Understanding laser powder bed fusion surface roughness, J. Manuf. Sci. Eng. 142 (2020) 071003, https://doi.org/10.1115/1.4046504.

[13] Y. Tian, D. Tomus, P. Rometsch, X. Wu, Influences of processing parameters on surface roughness of Hastelloy X produced by selective laser melting, Addit. Manuf. 13 (2017) 103–112, https://doi.org/10.1016/j.addma.2016.10.010.

[14] R. Li, J. Liu, Y. Shi, L. Wang, W. Jiang, Balling behavior of stainless steel and nickel powder during selective laser melting process, Int. J. Adv. Manuf. Technol. 59 (2012) 1025–1035, https://doi.org/10.1007/s00170-011-3566-1.

[15] D. Wang, Y. Liu, Y. Yang, D. Xiao, Theoretical and experimental study on surface roughness of 316L stainless steel metal parts obtained through selective laser melting, Rapid Prototyp. J. 22 (2016) 706–716, https://doi.org/10.1108/RPJ-06-2015-0078.

[16] S. Chowdhury, N. Yadaiah, C. Prakash, S. Ramakrishna, S. Dixit, L.R. Gupta, D. Buddhi, Laser powder bed fusion: a state-of-the-art review of the technology, materials, properties & defects, and numerical modelling, J. Mater. Res. Technol. 20 (2022) 2109–2172, https://doi.org/10.1016/j.jmrt.2022.07.121.

[17] I. Koutiri, E. Pessard, P. Peyre, O. Amlou, T. De Terris, Influence of SLM process parameters on the surface finish, porosity rate and fatigue behavior of as-built Inconel 625 parts, J. Mater. Process. Technol. 255 (2018) 536–546, https://doi.org/10.1016/J.JMATPROTEC.2017.12.043.

[18] C. Qiu, Z. Wang, A.S. Aladawi, M. Al Kindi, I. Al Hatmi, H. Chen, L. Chen, Influence of laser processing strategy and remelting on surface structure and porosity development during selective laser melting of a metallic material, Metall. Mater. Trans. A Phys. Metall. Mater. Sci. 50 (2019) 4423–4434, https://doi.org/10.1007/s11661-019-05348-0.

[19] E. Yasa, J. Deckers, J.P. Kruth, The investigation of the influence of laser re-melting on density, surface quality and microstructure of selective laser melting parts, Rapid Prototyp. J. 17 (2011) 312–327, https://doi.org/10.1108/13552541111156450.

[20] P. Lu, Z. Cheng-Lin, L. Hai-Yi, W. Liang, L. Tong, A new two-step selective laser remelting of 316L stainless steel: process, density, surface roughness, mechanical properties, microstructure, Mater Res Express 7 (2020) 056503, https://doi.org/10.1088/2053-1591/ab8b86.

[21] B. Nagarajan, Z. Hu, S. Gao, X. Song, R. Huang, M. Seita, J. Wei, Effect of in-situ laser remelting on the microstructure of SS316L fabricated by micro selective laser melting, in: S. Itoh, S. Shukla (Eds.), Advanced Surface Enhancement, Springer, Singapore, 2020, pp. 330–336, https://doi.org/10.1007/978-981-15-0054-1_35.

[22] A.G. Demir, B. Previtali, Investigation of remelting and preheating in SLM of 18Ni300 maraging steel as corrective and preventive measures for porosity reduction, Int. J. Adv. Manuf. Technol. 93 (2017) 2697–2709, https://doi.org/10.1007/s00170-017-0697-z.

[23] N.T. Aboulkhair, N.M. Everitt, I. Ashcroft, C. Tuck, Reducing porosity in AlSi10Mg parts processed by selective laser melting, Addit. Manuf. 1–4 (2014) 77–86, https://doi.org/10.1016/J.ADDMA.2014.08.001.

[24] E. Yasa, J.P. Kruth, J. Deckers, Manufacturing by combining selective laser melting and selective laser Erosion/laser re-melting, CIRP Ann. 60 (2011) 263–266, https://doi.org/10.1016/J.CIRP.2011.03.063.

[25] A. Boschetto, L. Bottini, D. Pilone, Effect of laser remelting on surface roughness and microstructure of AlSi10Mg selective laser melting manufactured parts, Int. J. Adv. Manuf. Technol. 113 (2021) 2739–2759, https://doi.org/10.1007/s00170-021-06775-3.

[26] Y.E. Zafer, S. Goel, A. Ganvir, A. Jansson, S. Joshi, Encapsulation of electron beam melting produced alloy 718 to reduce surface connected defects by hot isostatic pressing, Materials 13 (2020) 1226, https://doi.org/10.3390/MA13051226.

[27] W. Tillmann, C. Schaak, J. Nellesen, M. Schaper, M.E. Aydinöz, T. Niendorf, Functional encapsulation of laser melted Inconel 718 by arc-PVD and HVOF for post compacting by hot isostatic pressing, Powder Metall. 58 (2015) 259–264, https://doi.org/10.1179/0032589915Z.000000000250.

[28] H.Q. Li, H. Guo, F.L. Shen, D.J. Lou, W.L. Xia, X.Y. Fang, Tribological and corrosion performance of the plasma-sprayed conformal ceramic coating on selective laser melted CoCrMo alloy, J. Mech. Behav. Biomed. Mater. 119 (2021) 104520, https://doi.org/10.1016/J.JMBBM.2021.104520.

[29] D.M. Jafarlou, G. Ferguson, K.L. Tsaknopoulos, A.C. Chuang, A. Nardi, D. Cote, V. Champagne, I.R. Grosse, Structural integrity of additively manufactured stainless steel with cold sprayed barrier coating under combined cyclic loading, Addit. Manuf. 35 (2020) 101338, https://doi.org/10.1016/J.ADDMA.2020.101338.

[30] M. Bellippady, M. Florent, S. Björklund, X.H. Li, F. Robert, B. Kjellman, S. Joshi, N. Markocsan, Characteristics and performance of suspension plasma sprayed thermal barrier coatings on additively manufactured superalloy substrates, Surf. Coat. Technol. 472 (2023) 129926, https://doi.org/10.1016/j.surfcoat.2023.129926.

[31] L. Pawlowski, The Science and Engineering of Thermal Spray Coatings, Second edition, John Wiley and Sons, 2008, https://doi.org/10.1002/9780470754085.

[32] B. Zhang, L. Zhu, H. Liao, C. Coddet, Improvement of surface properties of SLM parts by atmospheric plasma spraying coating, Appl. Surf. Sci. 263 (2012) 777–782, https://doi.org/10.1016/J.APSUSC.2012.09.170.

[33] Ž. Dlouhá, M. Vostřák, J. Duliškovič, I. Zetková, T. Mařík, Adhesion of selected thermally sprayed coatings on additive manufactured maraging steel, J. Phys. Conf. Ser. 2572 (2023) 012006, https://doi.org/10.1088/1742-6596/2572/1/012006.

[34] G. Bolelli, M.F. Bonilauri, P. Sassatelli, F. Bruno, R. Franci, G. Pulci, F. Marra, L. Paglia, G.C. Gazzadi, S. Frabboni, L. Lusvarghi, Pre-treatment of selective laser melting (SLM) surfaces for thermal spray coating, Surf. Coat. Technol. 441 (2022) 128533, https://doi.org/10.1016/J.SURFCOAT.2022.128533.

[35] W. Tillmann, L. Hagen, C. Schaak, J. Laß, M. Schaper, K.P. Hoyer, M.E. Aydinöz, K. U. Garthe, Adhesion of HVOF-sprayed WC-co coatings on 316L substrates processed by SLM, J. Therm. Spray Technol. 29 (2020) 1396–1409, https://doi.org/10.1007/S11666-020-01081-Y.

[36] D. Garcia-Alonso, N. Serres, C. Demian, S. Costil, C. Langlade, C. Coddet, Pre−/during−/post-laser processes to enhance the adhesion and mechanical properties of thermal-sprayed coatings with a reduced environmental impact, J. Therm. Spray Technol. 20 (2011) 719–735, https://doi.org/10.1007/s11666-011-9629-x.

[37] A. Lamraoui, S. Costil, C. Langlade, C. Coddet, Laser surface texturing (LST) treatment before thermal spraying: a new process to improve the substrate-coating adherence, Surf. Coat. Technol. 205 (2010) S164–S167, https://doi.org/10.1016/J.SURFCOAT.2010.07.044.

[38] R. Kromer, S. Costil, C. Verdy, S. Gojon, H. Liao, Laser surface texturing to enhance adhesion bond strength of spray coatings – cold spraying, wire-arc spraying, and atmospheric plasma spraying, Surf. Coat. Technol. 352 (2018) 642–653, https://doi.org/10.1016/j.surfcoat.2017.05.007.

[39] V. Kumar, R. Verma, Effect of GNP and laser-surface texturing on HVOF sprayed WC10Co4Cr coatings for high-wear resistance, Tribol. Int. 178 (2023) 108057, https://doi.org/10.1016/J.TRIBOINT.2022.108057.

[40] V. Kumar, R. Verma, K. Chauhan, R. Kumar, Influence of laser texturing pre-treatment on HVOF-sprayed WC-10Co-4Cr+GNP coatings on AISI 304, Surf Topogr 10 (2022) 015052, https://doi.org/10.1088/2051-672X/AC5C68.

[41] S.S. Aulakh, G. Kaushal, Laser texturing as an alternative to grit blasting for improved coating adhesion on AZ91D magnesium alloy, Trans. IMF 97 (2019) 100–108, https://doi.org/10.1080/00202967.2019.1578562.

[42] B. Lafuente, R.T. Downs, H. Yang, N. Stone, The power of databases: the RRUFF project, in: T. Armbruster, R.M. Danisi (Eds.), Highlights in Mineralogical Crystallography, De Gruyter (O), Berlin, München, Boston, 2016, pp. 1–29, https://doi.org/10.1515/9783110417104-003.

[43] S. Sendino, S. Martinez, F. Lartategui, M. Gardon, A. Lamikiz, J.J. Gonzalez, Effect of powder particle size distribution on the surface finish of components manufactured by laser powder bed fusion, Int. J. Adv. Manuf. Technol. 124 (2023) 789–799, https://doi.org/10.1007/S00170-022-10423-9/FIGURES/10s.

[44] J. Liu, K. Zhao, X. Wang, H. Li, Effect of initial surface morphology and laser parameters on the laser polishing of stainless steel manufactured by laser powder bed fusion, Materials 17 (2024) 4968, https://doi.org/10.3390/MA17204968.

[45] J. Schanz, M. Hofele, S. Ruck, T. Schubert, L. Hitzler, G. Schneider, M. Merkel, H. Riegel, Metallurgical investigations of laser remelted additively manufactured AlSi10Mg parts: Metallurgische Untersuchungen von laserstrahlumgeschmolzenen additiv hergestellten AlSi10Mg Bauteilen, Mater. Wiss. Werksttech. 48 (2017) 463–476, https://doi.org/10.1002/mawe.201700039.

[46] G. Bolelli, L.M. Berger, T. Börner, H. Koivuluoto, L. Lusvarghi, C. Lyphout, N. Markocsan, V. Matikainen, P. Nylén, P. Sassatelli, R. Trache, P. Vuoristo, Tribology of HVOF- and HVAF-sprayed WC–10Co4Cr hardmetal coatings: a comparative assessment, Surf. Coat. Technol. 265 (2015) 125–144, https://doi.org/10.1016/J.SURFCOAT.2015.01.048.

[47] G. Bolelli, L.M. Berger, M. Bonetti, L. Lusvarghi, Comparative study of the dry sliding wear behavior of HVOF-sprayed WC–(W,Cr)2C–Ni and WC–CoCr hardmetal

coatings, Wear 309 (2014) 96–111, https://doi.org/10.1016/J.WEAR.2013.11.001.
[48] C. Verdon, A. Karimi, J.L. Martin, A study of high velocity oxy-fuel thermally sprayed tungsten carbide based coatings. Part 1: microstructures, Mater. Sci. Eng. A 246 (1998) 11–24, https://doi.org/10.1016/S0921-5093(97)00759-4.
[49] P.L. Fauchais, J.V.R. Heberlein, M.I. Boulos, Combustion spraying systems, in: Thermal spray fundamentals, 2014, pp. 227–303, https://doi.org/10.1007/978-0-387-68991-3_5.
[50] G. Bolelli, A. Milanti, L. Lusvarghi, L. Trombi, H. Koivuluoto, P. Vuoristo, Wear and impact behaviour of high velocity air-fuel sprayed Fe–Cr–Ni–B–C alloy coatings, Tribol. Int. 95 (2016) 372–390, https://doi.org/10.1016/J.TRIBOINT.2015.11.036.
[51] V. Testa, S. Morelli, G. Bolelli, B. Benedetti, P. Puddu, P. Sassatelli, L. Lusvarghi, Alternative metallic matrices for WC-based HVOF coatings, Surf. Coat. Technol. 402 (2020) 126308, https://doi.org/10.1016/J.SURFCOAT.2020.126308.
[52] J.M. Perry, A. Neville, V.A. Wilson, T. Hodgkiess, Assessment of the corrosion rates and mechanisms of a WC–Co–Cr HVOF coating in static and liquid–solid impingement saline environments, Surf. Coat. Technol. 137 (2001) 43–51, https://doi.org/10.1016/S0257-8972(00)01062-8.
[53] Y. Tian, H. Zhang, X. Chen, A. McDonald, S. Wu, T. Xiao, H. Li, Effect of cavitation on corrosion behavior of HVOF-sprayed WC-10Co4Cr coating with post-sealing in artificial seawater, Surf. Coat. Technol. 397 (2020) 126012, https://doi.org/10.1016/J.SURFCOAT.2020.126012.
[54] V.A.D. Souza, A. Neville, Mechanisms and kinetics of WC-Co-Cr high velocity oxy-fuel thermal spray coating degradation in corrosive environments, J. Therm. Spray Technol. 15 (2006) 106–117, https://doi.org/10.1361/105996306X92677.
[55] P. Sassatelli, G. Bolelli, M. Lassinantti Gualtieri, E. Heinonen, M. Honkanen, L. Lusvarghi, T. Manfredini, R. Rigon, M. Vippola, Properties of HVOF-sprayed Stellite-6 coatings, Surf. Coat. Technol. 338 (2018) 45–62, https://doi.org/10.1016/j.surfcoat.2018.01.078.